ORNL/TM-13283

OAK RIDGE NATIONAL LABORATORY

LOCKHEED MARTIN

PROSPECTS FOR CHAOS CONTROL OF MACHINE TOOL CHATTER

L. M. Hively
V. A. Protopopescu
N. E. Clapp
C. S. Daw
Oak Ridge National Laboratory

CAUTION

This document has not been given final patent clearance and is for internal use only. If this document is to be given public release, it must be cleared through the site Technical Information Office which will see that the proper patent and technical information reviews are completed in accordance with Lockheed Martin Energy Research Policy.

MANAGED AND OPERATED BY
LOCKHEED MARTIN ENERGY RESEARCH CORPORATION
FOR THE UNITED STATES
DEPARTMENT OF ENERGY

ORNL-27 (3-96)

This report has been reproduced directly from the best available copy.

Available to DOE and DOE contractors from the Office of Scientific and Technical Information, P. O. Box 62, Oak Ridge, TN 37831; prices available from (423) 576-8401.

Available to the public from the National Technical Information Service, U.S. Department of Commerce, 5285 Port Royal Rd., Springfield, VA 22161.

This report was prepared as an account of work sponsored by an agency of the United States Government. Neither the United States Government nor any agency thereof, nor any of their employees, make any warranty, express or implied, or assumes any legal liability or responsibility for the accuracy, completeness, or usefulness of any information, apparatus, product, or process disclosed, or represents that its use would not infringe privately owned rights. Reference herein to any specific commercial product, process, or service by trade name, trademark, manufacturer, or otherwise, does not necessarily constitute or imply its endorsement, recommendation, or favoring by the United States Government or any agency thereof. The views and opinions of authors expressed herein do not necessarily state or reflect those of the United States Government or any agency thereof.

ORNL/TM-13283

PROSPECTS FOR CHAOS CONTROL OF MACHINE TOOL CHATTER

L. M. Hively
V. A. Protopopescu
N. E. Clapp
C. S. Daw
Oak Ridge National Laboratory

June 1998

Prepared for
U.S. Department of Energy
Office of Defense Programs
under CRADA #Y1295-0357

Prepared by the
Engineering Technology Division
Oak Ridge National Laboratory
Oak Ridge, TN 37831-8066
managed by
LOCKHEED MARTIN ENERGY RESEARCH CORPORATION
for the
U.S. DEPARTMENT OF ENERGY
under contract DE-AC05-96OR22464

The submitted manuscript has been authored by a contractor of the U.S. Government under contract No. DE-AC05-96OR22464. Accordingly, the U.S. Government retains a nonexclusive, royalty-free license to publish or reproduce the published form of this contribution, or allow others to do so, for U.S. Government purposes.

CONTENTS

	Page
LIST OF FIGURE	v
LIST OF TABLES	vii
ABSTRACT	ix
1. INTRODUCTION	1
2. DATA ACQUISITION	4
3. FORMULATION OF CYCLE ENERGY	6
4. RESULTS	8
5. DISCUSSION	36
ACKNOWLEDGMENTS	37
REFERENCES	38

LIST OF FIGURES

Page

Fig. 2.1. Coordinate system (x, y, z) for the tool-part configuration 5

Fig. 3.1. Typical time-serial plots for dataset #091801..... 7

Fig. 4.1. Typical plots of machining power vs time..... 9

Fig. 4.2. Fourier spectrum of P 10

Fig. 4.3. Mutual information function of the power P 12

Fig. 4.4. Principal component plots for datasets #091801–091805 14

Fig. 4.5. Two-dimensional phase-space plots of the power P..... 15

Fig. 4.6. LOG_{10}(K) of P vs scale length..... 16

Fig. 4.7. Correlation dimension spectrum of the power P 18

Fig. 4.8. Return maps for E_i^+ (lag=1) 20

Fig. 4.9. Return maps for E_i^- (lag=1) 21

Fig. 4.10. Return map for E_i^- (lag=1) to and from the fixed point for dataset #091801 23

Fig. 4.11. Stable and unstable manifolds for E_i^- (lag=1) 24

Fig. 4.12. Period-1 return map for E_i^+ for dataset #091801 26

Fig. 4.13. Normalized period-m occurrence frequency vs m for $E_i^\pm$ 27

Fig. 4.14. Period-1 return maps for T_i^+ 28

Fig. 4.15. Period-2 return maps for T_i^+ 30

Fig. 4.16. Period-3 return maps for T_i^+ 31

Fig. 4.17. Period-1 return maps for T_i^-..... 32

Fig. 4.18. Period-2 return maps for T_i^-..... 33

Fig. 4.19. Normalized period-m occurrence frequency vs m for $T_i^\pm$ 34

Fig. 4.20. Period-1 return map for T_i^+ to and from the fixed point for dataset #091802 35

LIST OF TABLES

Page

Table 2.1. Summary of datasets 4

Table 4.1. Comparison of average cycle lengths 8

Table 4.2. Important frequencies from the Fourier spectra of the power P 11

ABSTRACT

We analyze the nonlinear tool-part dynamics during turning of stainless steel in the nonchatter and chatter regimes, toward the ultimate objective of chatter control. Our previous work in ORNL/TM-13157 [1] analyzed tool acceleration in three dimensions at four spindle speeds. In the present work, we analyze the machining power and obtain nonlinear measures of this power. We also calculate the cycle-to-cycle energy for the turning process. Return maps for power cycle times do not reveal fixed points or (un)stable manifolds. Energy return maps do display stable and unstable directions (manifolds) to and from an unstable period-1 orbit, which is the dominant periodicity. Both nonchatter and chatter dynamics have the unusual feature of arriving at the unstable period-1 fixed point and departing from that fixed point of the energy return map in a single step. This unusual feature makes chaos "maintenance," based on the well-known Ott–Grebogi–Yorke scheme, a very difficult option for chatter suppression. Alternative control schemes, such as synchronization of the tool-part motion to prerecorded nonchatter dynamics or dynamically damping the period-1 motion, are briefly discussed.

1. INTRODUCTION

Advanced machining requires faster material removal, which frequently causes poor part quality due to irregular, uncontrolled tool-part dynamics. For example, tool chatter results in nicks, gouges, rough surface finish, and more rapid tool wear. Such features are unacceptable from the standpoint of quality assurance and economic efficiency. This report studies theoretical prospects for chaos control of tool chatter to (i) provide consistently high part quality, (ii) enable faster material removal, (iii) reduce waste, and (iv) improve overall efficiency.

Machine tool analysis has been developed [1–28] in the framework of classical nonlinear dynamics. One early work [23] described cutting forces during chatter as "very complex" and "very far from sinusoidal." Tlusty [12, 18, 20] published extensive experimental stability diagrams for turning, milling, boring, hobbing, and planing showing chatter when the machining parameter(s) occur in the unstable region. Qu et al. [16] obtained various nonlinear measures of vibration data to diagnose dynamics of rotating machinery (turbogenerator and compressor). Bukkapatnam et al. [3] recently analyzed data from lathe cutting and found low-dimensional, chaotic features. In our previous work [1], we analyzed experimental dynamics during turning of stainless steel. We found that nonchatter cutting occurred at low-spindle speeds with multiple periodicities, low-acceleration amplitude, and strongly chaotic features. Chatter occurred at higher spindle speeds with high-acceleration amplitude, low complexity, weak chaotic features, and strong periodic dynamics. The transition from nonchatter to chatter cutting is dominated by motion along the axis of the cutting tool.

A simple, one-dimensional model for machine tool dynamics is a damped, driven, oscillator in the form of a delayed ordinary differential equation for the chip thickness (y) vs time (t):

$$A\, d^2y/dt^2 + B\, dy/dt + Cy = D[y(t-T) - y(t)] \,. \qquad (1.1)$$

The left-hand side of Eq. 1.1 describes tool acceleration (first term), velocity-dependent damping (second term), and tool force against the workpiece (third term). The right-hand side (RHS) accounts for the force from "regenerative chatter," which involves tool motion, y(t-T), during the previous cut that produces an undulated surface from which the present cut, y(t), removes a chip. The RHS of Eq. 1.1 is interpreted as zero for a negative time-delay difference and corresponds to the tool losing contact with the workpiece when chatter amplitude is above a critical amplitude [14]. Parameters (A, B, C, D) depend on the operation, geometry, part material, etc. The lag (T) is the time between successive cutting cycles (e.g., time per revolution in a turning operation).

The stability regimes of Eq.1.1 were analyzed by Stépán [17] and Chiriacescu [4]. Regenerative chatter models (e.g., Ref. 4) predict one (or more) instability region(s) in a phase space of cutting width vs rotation speed (Ω) for turning, tool spring constant vs Ω for milling, and feed rate vs Ω for drilling. This analysis also predicts one (or more) chatter regimes as Ω and feed rate increase. Stépán also discussed Tobias' improvement [21] to the model for dynamic damping by a modification to the driving force on the tool for turning, milling, and drilling. The improved model gave greater chatter stability at low-cutting speed in accord with

experiments. Stépán introduced a further improvement to the model with an additional (short) regeneration time as the chip moves over the tool cutting edge. This process distributes the force along the tool-chip interface, resulting in an integro-differential equation for the distributed time delay. That model predicted greater chatter stability at high-cutting speeds in accord with experiments. Jemielniak and Widota [10] used a linear model of random disturbances due to the unpredictability of chip removal, resulting in amplitude modulation of the tool motion. Moon [15] included a velocity-dependent friction and found loss of stability with increasing depth of cut, leading to chatter as a quasi-periodic tool motion.

Two-dimensional models for regenerative chatter involve cutting direction (x) and a cutting depth (y). Tool-workpiece contact causes mode coupling between the independent directions of motion, each with different frequencies, amplitudes, and phases. The workpiece imparts energy to the tool during one part of the cycle, and the tool gives energy to the chip and workpiece during another portion of the oscillation. Vibration amplitude grows if the net energy into the tool exceeds dissipative losses, thus producing unstable cutting. If friction and damping losses exceed the net energy into the tool, then the oscillation cannot grow, resulting in stable cutting. The "velocity component principle" is energy transfer due to any time-varying phase shift between chip thickness and cutting force in the y- and z-(feed) directions. Early two-dimensional modeling by Tlusty and Ismail [19] found that the tool can lose contact with the workpiece at large chatter amplitude, thus improving chatter stability for turning and milling. The nonlinear delayed differential equation (DDE) model of Wu and Liu [25] included fluctuations in the mean friction coefficient due to chip removal, and yielded results that are consistent with experimental chatter dynamics [26]. Berger et al. [2] used the model of Ref. 25 and found chaotic dynamics for certain parameter regimes, with limit cycle behavior in heavy chatter and more complex dynamics in mild chatter. Chaotic dynamics has also been found in related models [5, 22].

For completeness, we mention two other empirical models of machining dynamics. Grabec [6–8] used a pair of coupled nonlinear oscillators in the cutting direction (x) and depth of cut (y) with empirical models for the damping and driving forces and found chaotic features in the resulting dynamics. Hualing [9] included a nonlinear hysteretic restoring force and found a stability boundary that is consistent with observations.

A variety of approaches have been proposed to control or reduce chatter. See Refs. 29–56 on general control methods for chaotic systems and Refs. 57–58 for an extensive bibliography on chatter control. One standard technique selects machining parameters that avoid chatter operation. Another method [27] detects when the dominant chatter frequency crosses a threshold, then halts the milling feed, adjusts the spindle speed, and resumes the cut. Telz and Elbestawi [28] describe a controller for turning that maximizes feed within the constraints of tool breakage and edge chipping, that also adjusts the depth of cut to avoid chatter onset. Feedback control can dynamically damp the period-1 motion. Pratt and Nayfeh [57–58] showed biaxial suppression of boring-bar chatter with an active vibration absorber that employed reaction mass actuators. A very recent approach [59] vibrates the tool at a frequency equal in amplitude, but opposite in phase, to the cutting vibration of boring bars, thereby extending chatter thresholds up to 400%.

Robust and efficient chatter control is rendered very difficult by friction, noise, and discrete chip removal due to discontinuous behavior [40]. Moreover, prolonged chatter frequently enhances tool wear, which may cause a threshold change for chatter, thus complicating control further. Therefore, delay coordinate methods [e.g., Refs. 41–43] appear inappropriate for control of discontinuous systems. Feedback control cannot ignore noise in targeting and stabilization requiring frequent changes for efficient chatter suppression or enhancement. Another chatter control alternative is based on the enhancement of low-amplitude chaos along the tool axis, by synchronization of the tool-part motion to prerecorded nonchatter motion. However, such methods must balance the competition between chaos and nonlinear dynamic damping. For example, Boffetta et al. [56] show examples of driver-slave systems that would not be amenable to synchronization or entrainment.

In this work, we study nonlinear features of cutting power and energy to evaluate the prospects of chaos control of tool chatter by the Ott–Grebogi–Yorke scheme. See Ref. 48 for an extensive discussion of this method and related bibliography. This approach appears both feasible and reasonable, based on substantial experimental successes for both low- and high-dimensional processes [29–33]. Moreover, the method requires rather precise determination of the stable and unstable manifolds, which we discuss in the present work.

This paper is organized as follows. Section 2 explains the data acquisition. Section 3 describes the formulation of machining power and cycle-to-cycle energy. Section 4 presents our results, including return maps for the cycle-to-cycle tool energy. Section 5 discusses the implications of our work.

2. DATA ACQUISITION

We obtained data during turning of a 316 stainless steel cylinder on a lathe (Monarch Mark Century 2000) in Building 9737 at the Y-12 Plant in Oak Ridge, Tennessee. The cutting tool was a diamond-shaped carbide insert. The analog-to-digital converter recorded the data with 12-bit precision (i.e., values between –2048 and +2047). The acceleration data were given in arbitrary units, so all subsequent results are in arbitrary units (AU). The data sampling rate was 50 kilohertz) for each of the three orthogonal accelerations (A) in the (x, y, z) directions: A_x, A_y, A_z. The accelerometer accuracy was $\pm 2\%$ accuracy at ≤ 7 kilohertz, rising to $\pm 5\%$ accuracy for ≤ 10 kilohertz. Accelerometer calibration above 10 kilohertz was unavailable. The coordinate system is fixed with respect to the tool and has "x" along the cutting direction, "y" along the tool axis, and "z" along the feed direction which is also the axis about which the turning occurs (see Fig. 2.1).

Table 2.1 summarizes the parameters for five datasets of stainless steel machining (0.3048-mm feed rate per revolution, 0.254-millimeter depth of cut), at spindle speeds of 75, 100, 125, and 150 rpm. Datasets #091802 and #091803 were at the same spindle speed (100 rpm) and showed consistent results [1]. The principal Fourier frequency (f_p) increases monotonically with spindle speed for all three components of the acceleration. The number of timesteps per cycle (T_c) measures the average cycle period. $T_c(A_x)$ and $T_c(A_z)$ decrease with increasing spindle speed, but $T_c(A_y)$ is nonmonotonic. The acceleration amplitude range (ΔA_i) is the difference between the largest and smallest value of each acceleration component (A_i) for i = (x, y, or z). ΔA_y rises as the spindle speed increases, with the two largest values corresponding to the chatter regime. The amplitude range in the other two channels (ΔA_x and ΔA_z) is nonmonotonic.

Table 2.1. Summary of datasets

	Dataset				
Parameter	091801	091802	091803	091804	091805
Spindle speed (rpm)	75	100	100	125	150
Cutting regime	nonchatter	nonchatter	nonchatter	chatter	chatter
$f_p(A_x)$ (Hz)	1514	1526	1538	1563	1575
$f_p(A_y)$ (Hz)	1514	1526	1538	1563	1575
$f_p(A_z)$ (Hz)	3027	3064	3064	3113	3149
$T_c(A_x)$ (timesteps/cycle)	33.0	32.7	32.6	32.1	31.7
$T_c(A_y)$ (timesteps/cycle)	26.2	27.3	30.7	32.1	31.7
$T_c(A_z)$ (timesteps/cycle)	16.5	16.3	16.3	16.0	15.9
ΔA_x (AU)	584	479	433	474	387
ΔA_y (AU)	169	219	178	272	387
ΔA_z (AU)	172	154	115	153	178

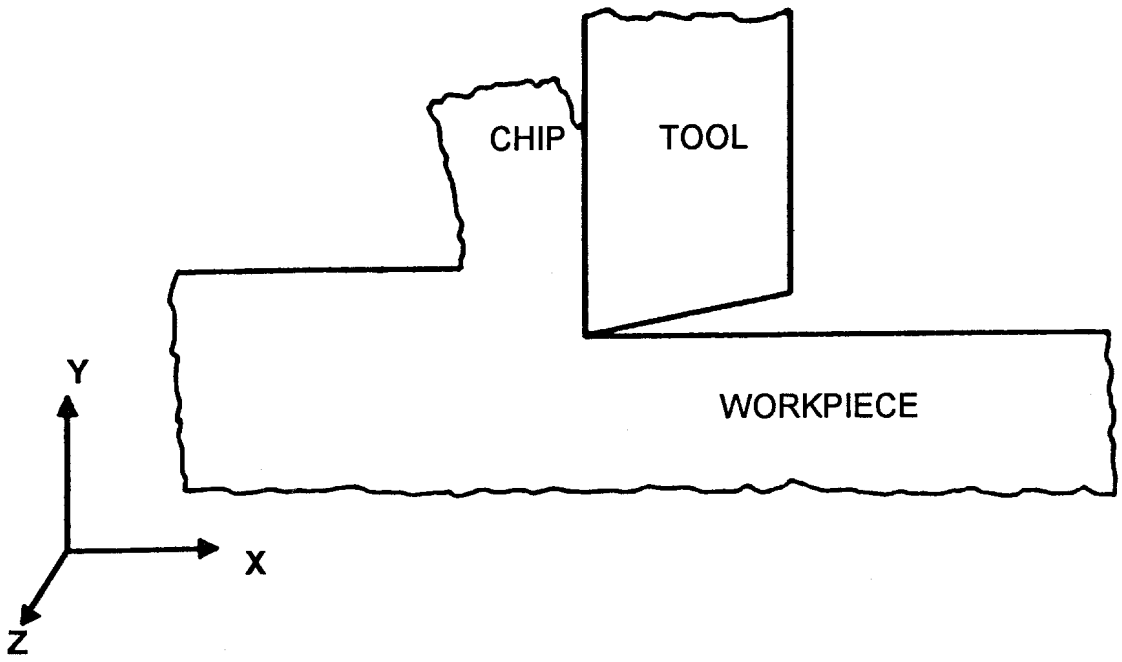

Fig. 2.1. Coordinate system (x, y, z) for the tool-part configuration.

3. FORMULATION OF CYCLE ENERGY

Previous experience revealed a fruitful line of analysis by characterizating each cycle of a process by a single nonlinear measure. For example, cycle-to-cycle analysis in an internal combustion engine showed that chaos in lean-burn dynamics arises from the carry-over of combustion products from the previous cycle [37]. Typical cycle-to-cycle measures in a mechanical system are particles (or mass), momentum, and energy. Regarding mass, the large-scale metal removal rate is set by the cutting parameters (depth of cut, feed rate, width of cut, and spindle speed), but microscopic variations are very difficult to measure with sufficient speed and accuracy. Regarding momentum, our previous work [1] showed that all three components of acceleration are necessary to characterize tool chatter. Rather, we use energy as a single integral quantity to characterize the cycle-to-cycle cutting dynamics.

Energy (E_i) is the time integral over the i-th power cycle ($P = \mathbf{F} \cdot \mathbf{V}$) with the raised dot denoting vector dot product between vector quantities (denoted by bold-face symbols). Here, **F** is the force vector, which is the product of tool mass, m, and acceleration, **A**. **V** is the velocity vector, which is the time integral of acceleration. Combining these quantities yields:

$$V_k = \int A_k \, dt \, , \tag{3.1}$$

$$P = \mathbf{F} \cdot \mathbf{V} = m \, (A_x V_x + A_y V_y + A_z V_z) \, , \tag{3.2}$$

$$E_i = \int P \, dt = m \int (A_x V_x + A_y V_y + A_z V_z) \, dt \, . \tag{3.3}$$

The index k in Eq. 3.1 corresponds to the three orthogonal components (x, y, and z) of acceleration and velocity. Figure 3.1(a) shows a typical time-serial plot of A_y (solid curve). Numerical integration at the lowest order (trapezoidal rule) yields a nonphysical, continuous decrease in the average velocity, as illustrated by the dot-dashed curve in Fig. 3.1(a). Moreover, fourth-order integrators [38] yield the same continuous shift in average velocity (not shown). Since the divergence does not depend on the integration method, it most likely arises from unspecified systematic errors in the acceleration data, which we cannot correct after the fact. We remove this divergence in velocity via a zero-phase, quadratic filter [39] with a filter-window width of 1001 points, corresponding to 60–85 cycles in velocity dynamics. This filter removes offsets (e.g., due to the initial conditions of velocity integration, which are unknown) and eliminates the continuous decrease in average velocity (due to the systematic errors in the data). After this filtering operation, V_k and P vary smoothly about zero during the entire time history for all of the datasets [Fig. 3.1(b)]. Subsequent analysis uses only the filtered velocities and power.

We used zero-crossings in the power ($P = 0$) to determine the integration (cycle) times. In particular, we found positive-going zero-power crossings (i.e., changes from $P<0$ to $P>0$), and then obtained the corresponding times for zero-power crossings (t_i^+) by linear interpolation. Integration for positive-starting cycle energy (E_i^+) begins at t_i^+ and ends at t_{i+1}^+, as illustrated in Fig. 3.1(c). Likewise, we found negative-going zero-power crossings (i.e., changes from $P>0$ to $P<0$) and the corresponding times for zero-power crossings (t_i^-), with the integration time from t_i^- to t_{i+1}^- for the negative-starting cycle energy (E_i^-), also as shown in Fig. 3.1(c).

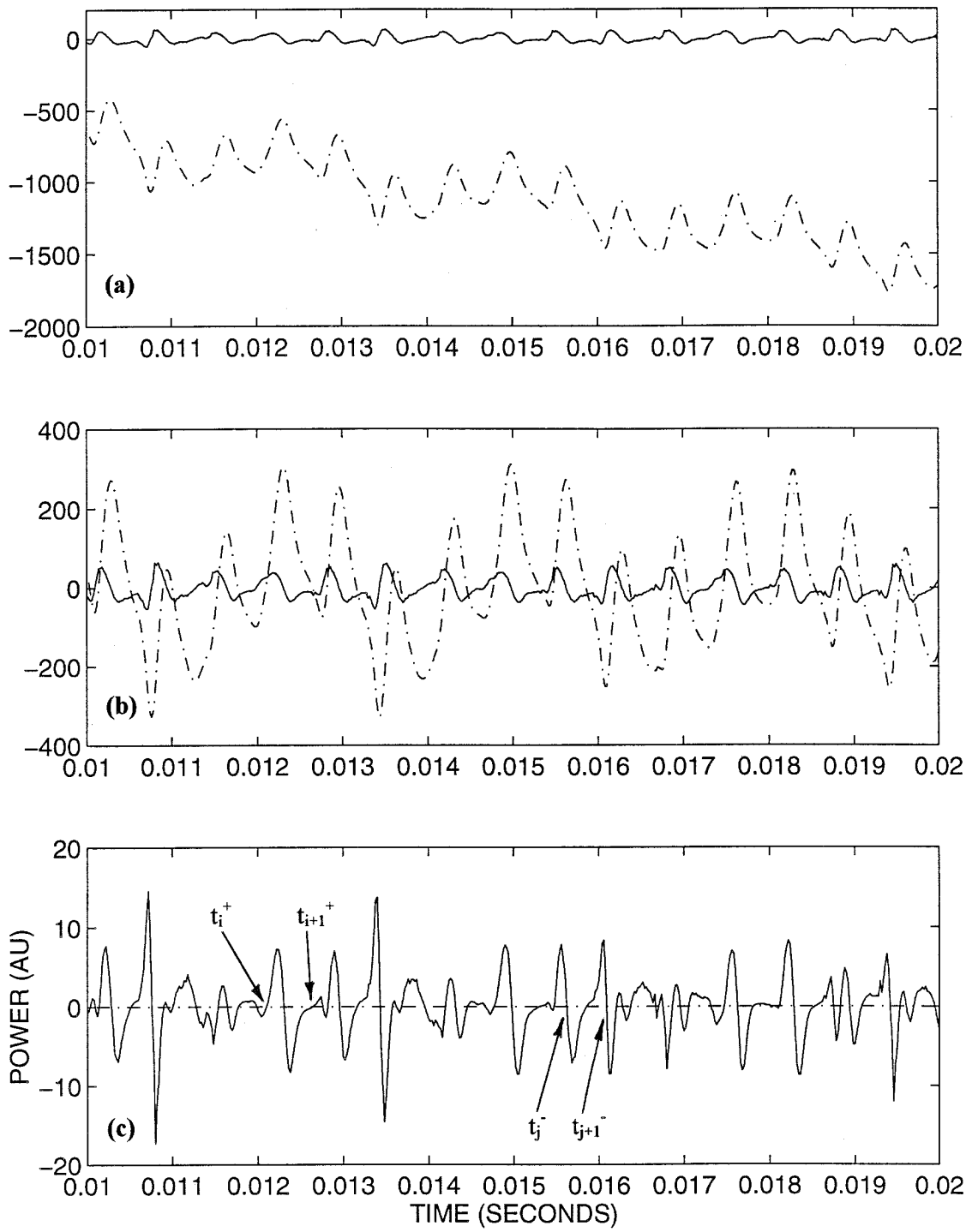

Fig. 3.1. Typical time-serial plots for dataset #091801 of (a) A_y (solid curve) and V_y (-·-) from Eq. 3.1, (b) A_y (solid curve) and V_y (-·-) after filtering, and (c) power (solid curve) and the line P=0 (-·-) for determination of zero-power crossings (see text for discussion).

4. RESULTS

Table 4.1 summarizes the characteristics of chatter acceleration and velocity. In particular, we compare the average cycle time from Table 2.1 for accelerations, $T_c(A_k)$, with the average cycle time for power, $T_c(P)$. We note that the cycle times for power are identical to $T_c(A_z)$ in the nonchatter regime (datasets #091801–091803), but are very different from any acceleration cycle times during chatter (datasets #091804–091805).

Table 4.1. Comparison of average cycle lengths

	Dataset				
Parameter	091801	091802	091803	091804	091805
Spindle speed (rpm)	75	100	100	125	150
Cutting regime	nonchatter	nonchatter	nonchatter	chatter	chatter
$T_c(A_x)$ (timesteps/cycle)	33.0	32.7	32.6	32.1	31.7
$T_c(A_y)$ (timesteps/cycle)	26.2	27.3	30.7	32.1	31.7
$T_c(A_z)$ (timesteps/cycle)	16.5	16.3	16.3	16.0	15.9
$T_c(P)$ (timesteps/cycle)	16.5	16.3	16.3	13.2	11.8

Figure 4.1 shows typical plots of power (P) for the five datasets. The top plot at 75 rpm [dataset #091801 in Fig. 4.1(a)] is farthest from chatter and has the lowest power variation ($\pm$17 AU). This power also has the most complex waveform, arising from strong chaotic features in the tool-part interaction. The second and third plots from the top at 100 rpm [datasets #091802–091803 in Figs. 4.1(b) and 4.1(c), respectively] are barely in the nonchatter regime and have slightly larger power variation ($\pm$19 AU). These powers have a less complex waveform, indicating weaker chaotic features. The fourth plot at 125 rpm [dataset #091804 in Fig. 4.1(d)] is barely into chatter and has a larger power variation ($\pm$29 AU). This power has rhythmic features indicating the presence of periodic (chatter) motion. The bottom plot at 150 rpm [dataset #091805 in Fig. 4.1(e)] is well into chatter and has the largest power variation ($\pm$50 AU). The power for this last dataset has the strong periodic features of chatter motion that can create poor quality cutting of the workpiece and excessive tool wear.

Figure 4.2 shows the Fourier spectrum of the power P for the five datasets. The top plot at 75 rpm [dataset #091801 in Fig. 4.2(a)] has many peaks, indicating chaotic competition among many different frequencies and no significant peaks above 12 kilohertz. The second and third plots at 100 rpm [datasets #091802–091803 in Figs. 4.2(b) and 4.2(c), respectively) show fewer distinct peaks. The largest peak occurs at 3 kilohertz, with secondary peaks at 1.5, 4.5, 6.1, and subsequent intervals of 1.5 kilohertz. Other (side-band) peaks occur at ~320 hertz above and below these important frequencies. Some significant frequency peaks occur above 12 kilohertz, particularly in Fig. 4.2(c), also at intervals of 1.5 kilohertz. The fourth plot at 125 rpm [dataset #091804 in Fig. 4.2(d)] has even sharper peaks at roughly the same frequencies, with clear peaks above the noise floor at frequencies above 12 kilohertz. The bottom plot at 150 rpm [dataset

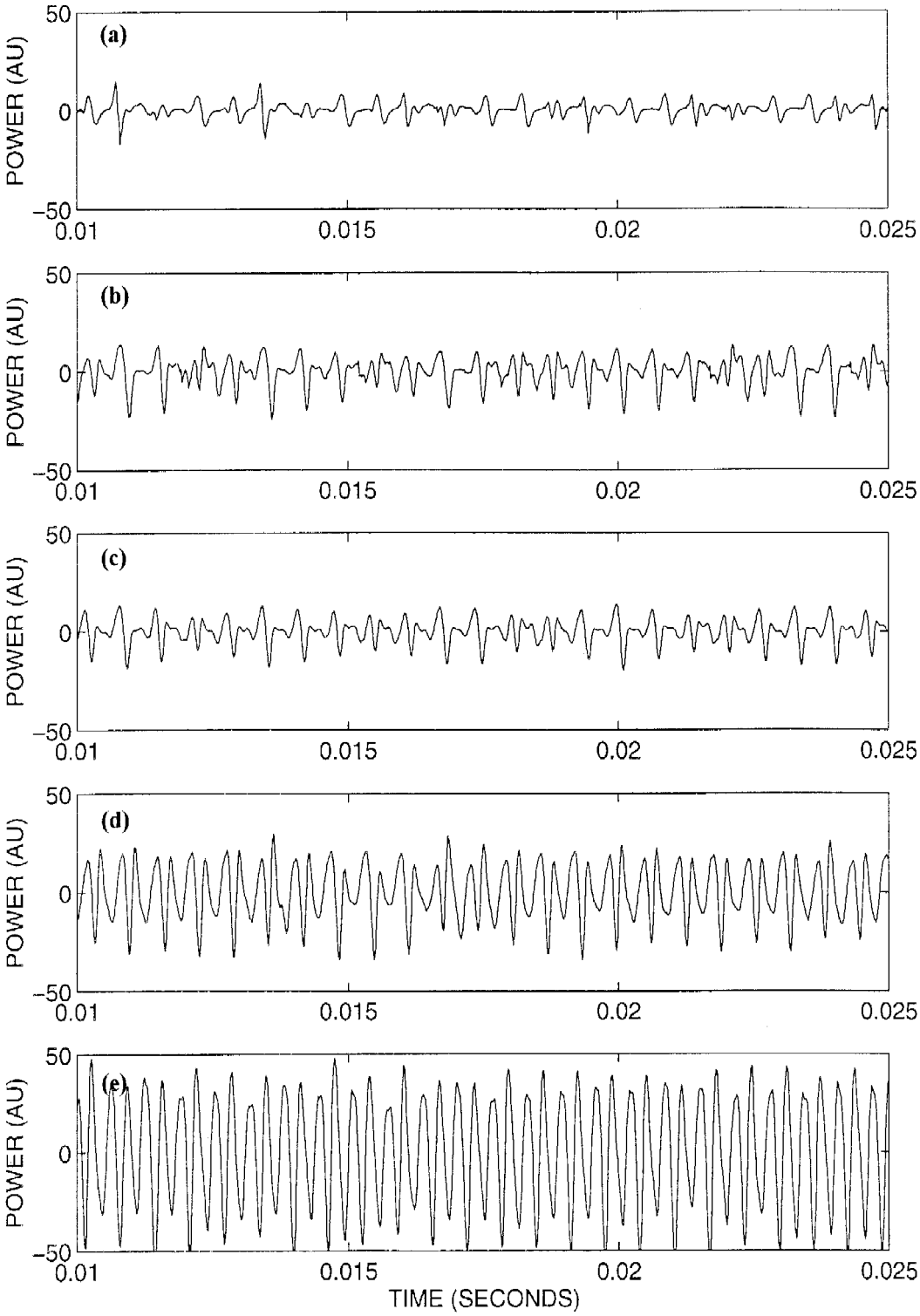

Fig. 4.1. Typical plots of machining power vs time at (a) 75 rpm, (b) 100 rpm (dataset #091802), (c) 100 rpm (dataset #091803), (d) 125 rpm, (e) 150 rpm.

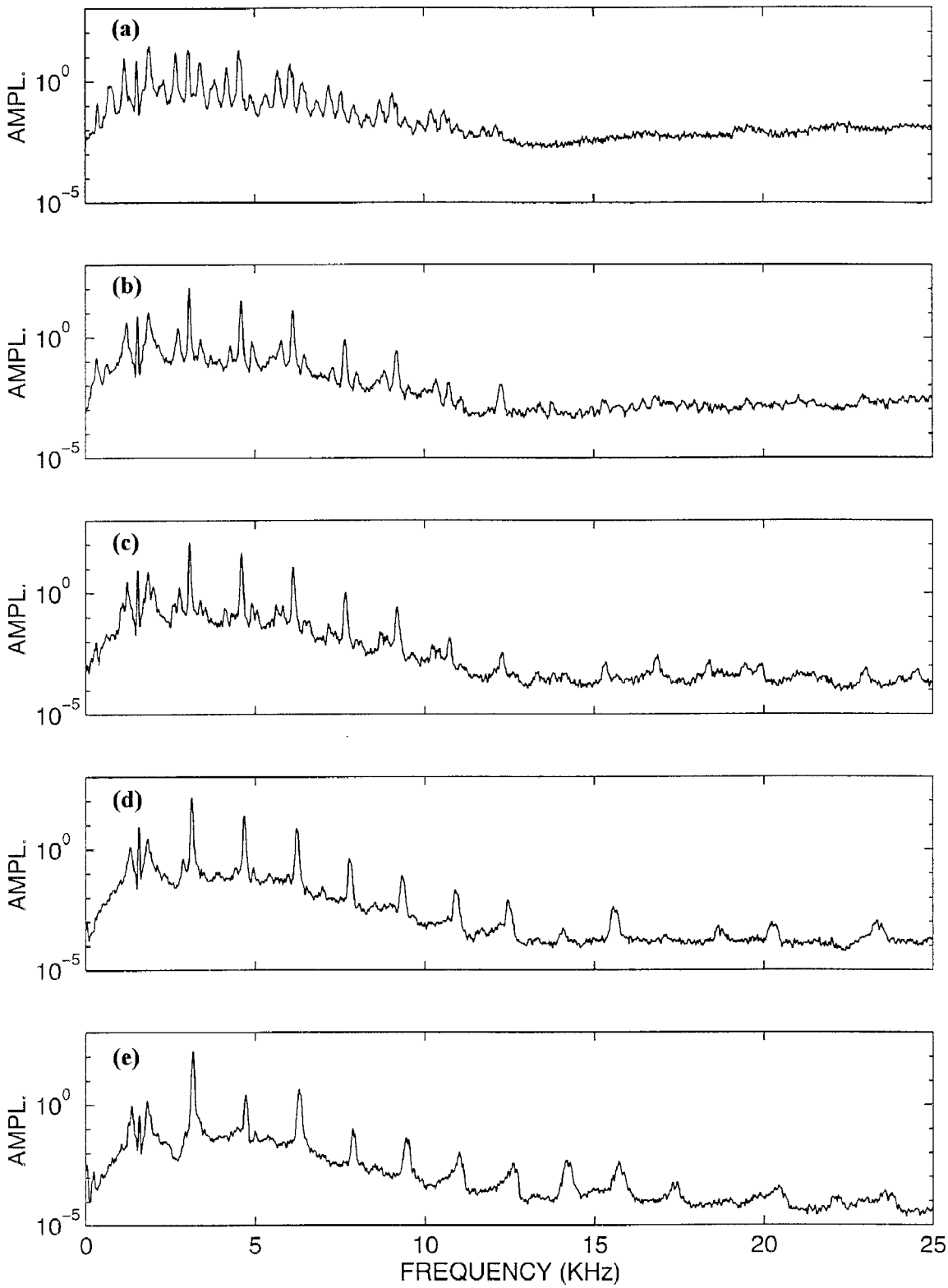

Fig. 4.2. Fourier spectrum of P at (a) 75 rpm, (b) 100 rpm (dataset #091802), (c) 100 rpm (dataset #091803), (d) 125 rpm, (e) 150 rpm.

#091805 in Fig. 4.2(e)] has very sharp peaks and very little side-band structure, also with clear peaks above the noise floor at frequencies above 12 kilohertz. The important peaks in these plots correspond exactly with the values in Table 4.1, as shown in Table 4.2 (below).

Table 4.2. Important frequencies from the Fourier spectra of the power P

	Dataset				
Parameter	091801	091802	091803	091804	091805
Spindle speed (rpm)	75	100	100	125	150
Cutting regime	nonchatter	nonchatter	nonchatter	chatter	chatter
$f_p(A_x)$ (Hz)	1514	1526	1538	1563	1575
$f_p(A_y)$ (Hz)	1514	1526	1538	1563	1575
$f_p(A_z)$ (Hz)	3027	3064	3064	3113	3149
Fourier peaks (Hz)	1148	1209	1221	1306	1355
	1514	1526	1538	1563	1575
	1880*	1856	1843	1819	1807
	3027	3064*	3064*	3113*	3149*
	4541+	4589+	4602+	4675+	4724
	6055	6128	6128	6226	6299+

* Indicates largest-amplitude peak in Fourier spectrum of machining power.
+ Indicates second largest-amplitude peak in Fourier spectrum of machining power.

We also obtained nonlinear measures of the machining power. Specifically, we determined the mutual information function, correlation dimension spectrum, entropy spectrum, principal components, phase-space plots, and return maps. Our previous work [1] explained the meaning of and methodologies for these measures, so we will not repeat that discussion here.

Figure 4.3 shows the mutual information function (MIF) for each dataset. The top plot [Fig. 4.3(a) at 75 rpm] has a few isolated peaks and little structure, indicating chaotic (nonchatter) cutting. The second and third plots [Figs. 4.3(b)–4.3(c) at 100 rpm) have a repetitive structure with many peaks and valleys, as precursors to chatter, even though these data are for nonchatter cutting. The fourth plot [Fig. 4.3(d) at 125 rpm] has a periodic structure of one large peak followed by three lower peaks showing that the tool-part motion is in mild chatter. The bottom plot [Fig. 4.3(e) at 150 rpm] has the same periodic structure as Fig. 4.3(d) for lag values <300 timesteps, then has a sequence of evenly spaced, monotonically decreasing peaks for lag values >300 timesteps. The maximum MIF value at zero lag is 2.81, 3.50, 3.80, 3.94, and 4.46 bits for 3.80, for datasets #091801–091805, respectively, and might be used as simple chatter detector. The first minimum always occurs at a lag of four timesteps.

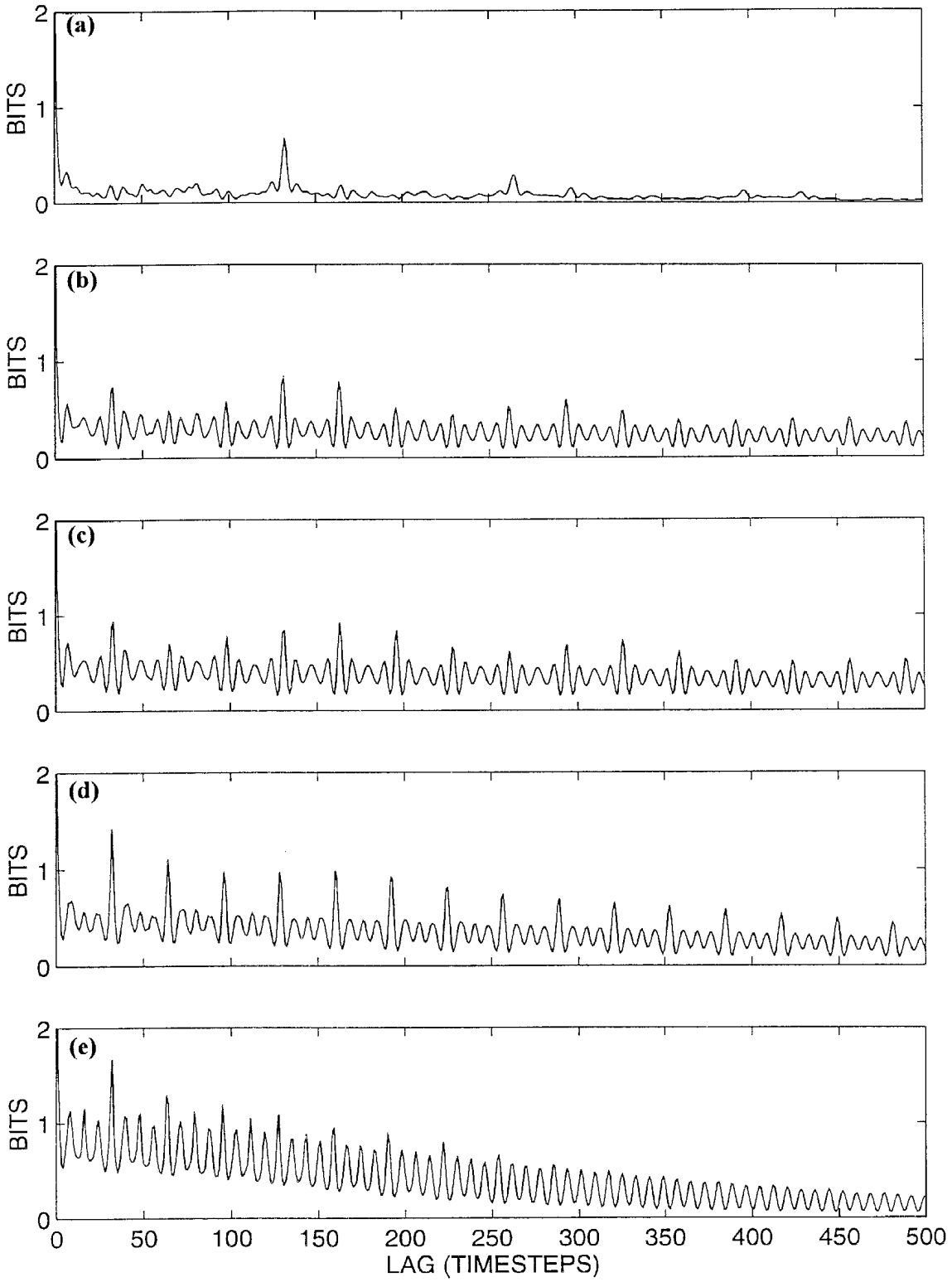

Fig. 4.3. Mutual information function of the power P at (a) 75 rpm, (b) 100 rpm (dataset #091802), (c) 100 rpm (dataset #091803), (d) 125 rpm, (e) 150 rpm.

Figure 4.4 shows principal component (PC) plots of machining power for each dataset. The principal components are rank ordered according to the size of the eigenvalue of the average correlation matrix of P, corresponding to the largest (PC1), second largest (PC2), and third largest (PC3) eigenvalues, respectively. The left, middle, and right column of plots show PC2 vs PC1, PC3 vs PC1, and PC3 vs PC2, respectively. The first through fifth row of plots show the plots for datasets #091801–091805, respectively. These figures display a clear structure in the dynamics of P, as a visualization (attractor) of the motion. The first two principal components (left column) reveal the clearest noise-filtered structure, which is the focus of the subsequent discussion. In Fig. 4.4(a) (75 rpm), two different heart-shaped figures (lying on their sides) are joined at their vertices, along with other loop-like structures, indicating several periodicities that contribute to the strong chaotic features of nonchatter cutting. In Figs. 4.4(d) and 4.4(g) (100 rpm), the motion takes the form of a large outer loop that is joined at the vertex by an inner (secondary) loop, as a period-2 orbit. In Fig. 4.4(j) (125 rpm), the motion is predominantly in the large outer loop, connecting to a slightly smaller inner loop that shows the periodic nature of slight chatter. In Fig. 4.4(m) (150 rpm), the chatter motion is a simple, almost circular period-1 orbit. The third PC (middle and right columns) is very complex, indicating the presence of some chaotic features even during chatter. We also changed the scale of the axes in these figures to show the most detail. Nonchatter plots [Figs. 4.4(a)–4.4(i)] have low variability, while the chatter plots [Figs. 4.4(j)–4.4(o)] have large variability, consistent with the power data in Fig. 4.1.

Figure 4.5 shows two-dimensional phase-space diagrams of P(t+L) vs P(t). The lag (L) is equal to the position of the first minimum in the MIF (L = 4 as discussed above). These figures also illustrate the attractor structure. Figure 4.5(a) shows the phase-space diagram for 75 rpm as a large, pointy heart-shaped figure (diagonally oriented), jointed at the vertex with a smaller rounded heart-shaped figure, plus other looping motion near the vertex. Figures 4.5(b)–4.5(c) (100 rpm) also show heart-shaped attractors (diagonally oriented) with noisy loops at the vertex. Figure 4.5(d) (125 rpm) depicts the mild chatter motion as a periodic double loop. Figure 4.5(e) illustrates the chatter motion at 150 rpm as a single periodic loop. These phase-space forms are consistent with the principal component plots without inherent noise filtering.

Figure 4.6 shows the Kolmogorov entropy (K) vs scale length for each dataset. K measures the loss of predictability in bits per timestep, which is largest at small-scale length (high unpredictability for noise) and smallest for global scales (good predictability for overall motion). Short-scale length corresponds to small changes (noise) in P, while large-scale length characterizes global motion of P. We measure scale length in units of the absolute average deviation (AAD) as a robust measure of variability:

$$\mathrm{AAD} = (1/N)\sum_{i=1}^{N} \left|x_i - \underline{x}\right| . \tag{4.1}$$

Here, x_i is the value of the observable (power in this case) at the time t_i , and $\underline{x}$ is the average of the observable (average of P in this case). The error bars in these figures indicate the 95% confidence interval for each sampling estimate of K. Figure 4.6(a) (75 rpm for nonchatter) shows that K decreases by slightly more than 10-fold as scale length (S) increases from 1 to 7 AADs. Figures 4.6(b)–4.6(c) (100 rpm for nonchatter) show a decrease in K of more than two decades as S rises from 1 to 7 AADs. Figure 4.6(d) (125 rpm for mild chatter) shows K decreasing by more than four decades as S rises from 1 to 7 AADs. Figure 4.6(e) (150 rpm for strong

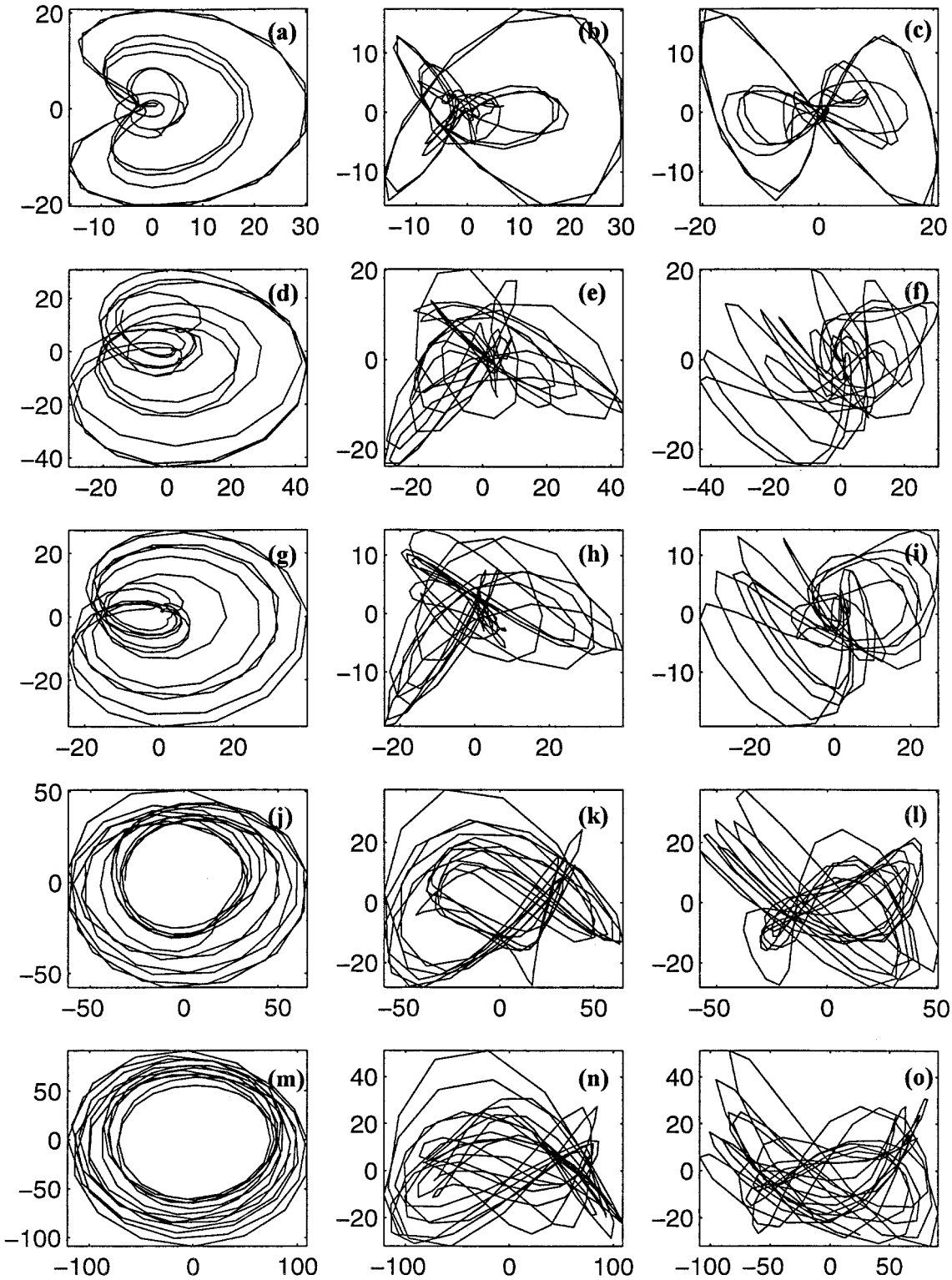

Fig. 4.4. Principal component plots for datasets #091801–091805 (see text for discussion).

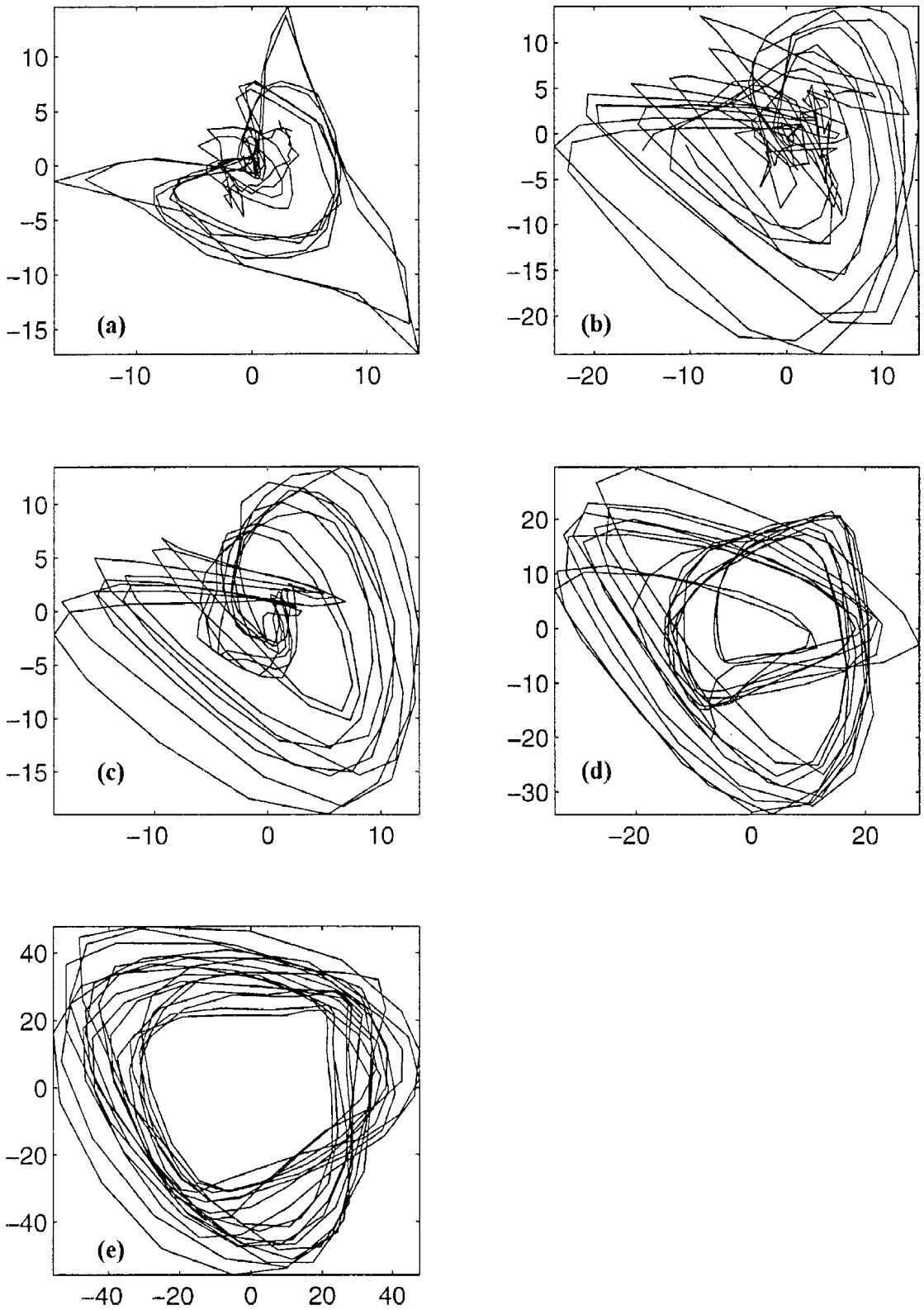

Fig. 4.5. Two-dimensional phase-space plots of the power P for (a) 75 rpm, (b) 100 rpm (dataset #091802), (c) 100 rpm (dataset #091803), (d) 125 rpm, (e) 150 rpm.

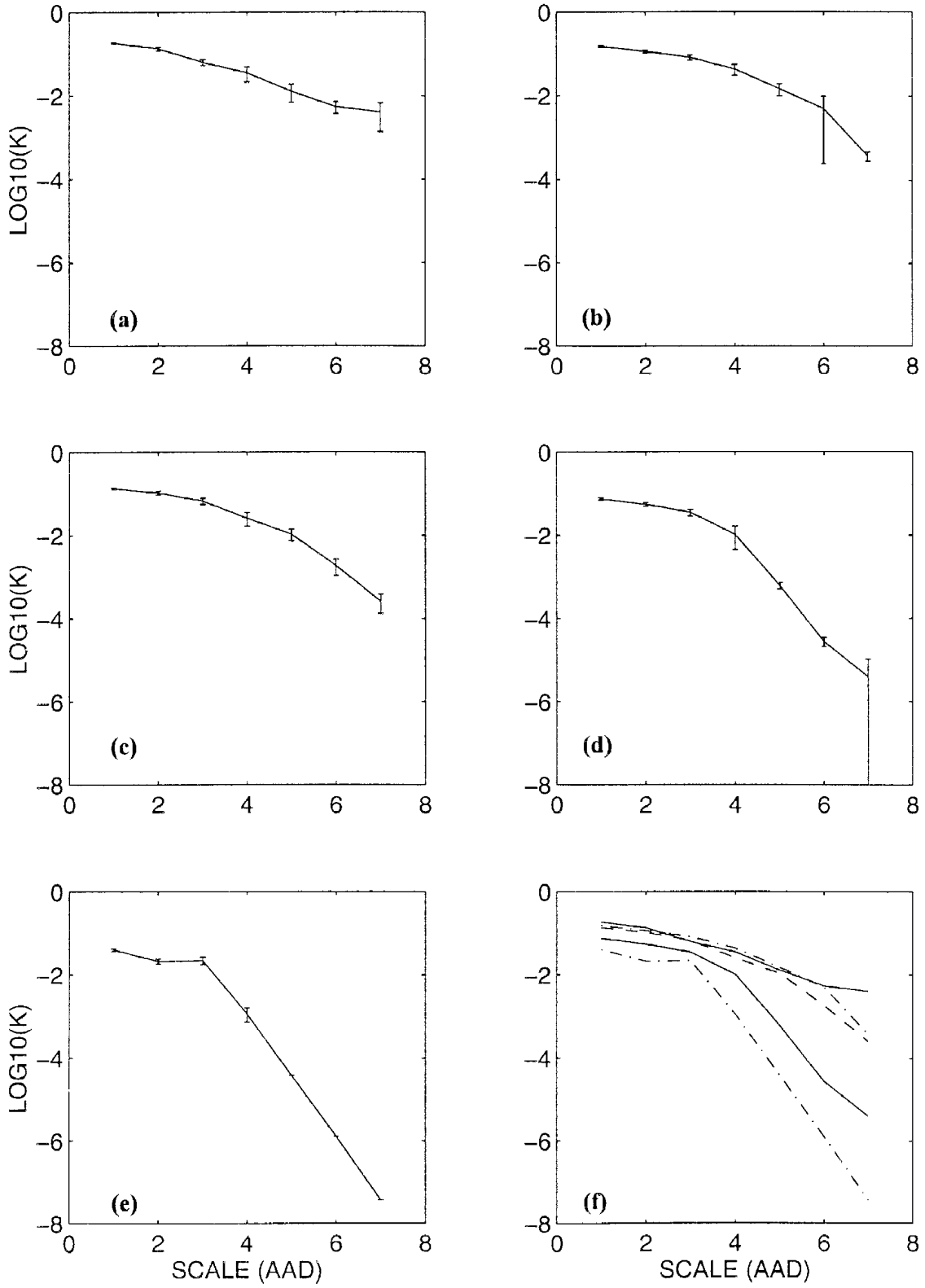

Fig. 4.6. $LOG_{10}(K)$ of P vs scale length for (a) 75 rpm, (b) 100 rpm (dataset #091802), (c) 100 rpm (dataset #091803), (d) 125 rpm, (e) 150 rpm, (f) composite.

chatter) shows a flat region (1 < S < 3 AADs) of large unpredictability, followed by a six-decade decrease in K as S increases to 7 AADs. Figure 4.6(f) is a composite of the previous five subplots. The upper solid curve is from Fig. 4.6(a) (75 rpm). The dot–dash (-·-) and dashed (- -) curves (100 rpm) are from Figs. 4.6(b)–4.6(c), respectively. The bottom solid curve (125 rpm) is from Fig. 4.6(d). The bottom dot–dash (-·-) curve (150 rpm) originates from Fig. 4.6(e). This composite shows that K progresses from flat and less predictable (strong chaotic features during nonchatter cutting) to steeply decreasing and predictable for (periodic) chatter cutting.

This analysis reveals the dynamical structure of P (Figs. 4.4–4.5), as well as at least one positive Lyapunov exponent, since K is the sum of the positive Lyapunov exponents (Fig. 4.6). These two measures (structure and positive Lyapunov exponent) provide a clear indication of chaos in cutting. Another important feature of chatter chaos is dimensionality, which we measure by the correlation dimension (CD) spectrum. Figure 4.7 shows CD vs scale length (S) for each dataset, with the error bars indicating the 95% confidence interval and S measured in AAD units. The organization of these plots is identical to that of Fig. 4.6. Large dimensionality (CD > 4) and large error bars occur at small S (the noisy domain). Small dimensionality (CD ~ 1) and small error bars exist at large S (the region of global motion). These figures also display a local plateau [Fig. 4.7(a)] or a local maximum and a local minimum in CD at intermediate S [Figs. 4.7(b)–4.7(e)]. This feature indicates that interesting and moderate-dimensional behavior in P (3.5 < CD < 1.5) occurs for scale lengths, 1 < S < 4 AAD. Figure 4.7(f) is a somewhat expanded composite plot of the CD spectra with the same organization as in Fig. 4.6(f). Nonchatter curves lie above the chatter curves for S > 2.5 AAD. CD at large-scale length (S = 7 AAD) is below unity during chatter but is above unity during nonchatter cutting. These trends are consistent with the previous results of greater nonchatter complexity (strong chaotic features) and lower chatter complexity (weak chaotic features and strong periodicity).

We next analyze the cycle-to-cycle energy. Evaluation of Eq. 3.3 for each positive- and negative-starting power cycle, respectively, yields E_i^+ or E_i^- to characterize the i-th cycle. Evaluation of Eq. 3.3 over each power cycle produces two, discrete time-serial sequences, $\{E_1^+, E_2^+, \ldots, E_n^+\}$ and $\{E_1^-, E_2^-, \ldots, E_n^-\}$. These sequences move from one unstable periodicity to another in recurring patterns that are driven by the tool-part nonlinearity. We visualize these patterns in a "return map" by plotting the energies in pairs (E_{i+m} vs E_i). Points near the diagonal, $E_{i+m} = E_i$, correspond to period-m motion because this location is visited every m-th cycle. Such points are also "unstable" because the system does not remain there, and "fixed" because the period-m location(s) do not change during repeated visits. Chaotic systems have an infinite number of unstable, periodic, fixed points. Moreover, stable and unstable directions span the region near an unstable fixed point in the shape of a multidimensional saddle. Return-map points approach an unstable fixed point along a locally linear "stable" direction (or manifold), like a ball rolling stably toward the center of a saddle. Return-map points depart from an unstable fixed point along a locally linear "unstable" direction (or manifold), like a ball rolling rapidly off the side of a saddle. The distance between the fixed point and successive departing points increases exponentially, displaying sensitivity to initial conditions which is the hallmark of chaos. Characterization of this topology requires analysis of the data for multiple approaches to and departures from the same fixed point along the same directions. Chatter control might exploit this topology to enhance chaotic behavior at the expense of periodic behavior.

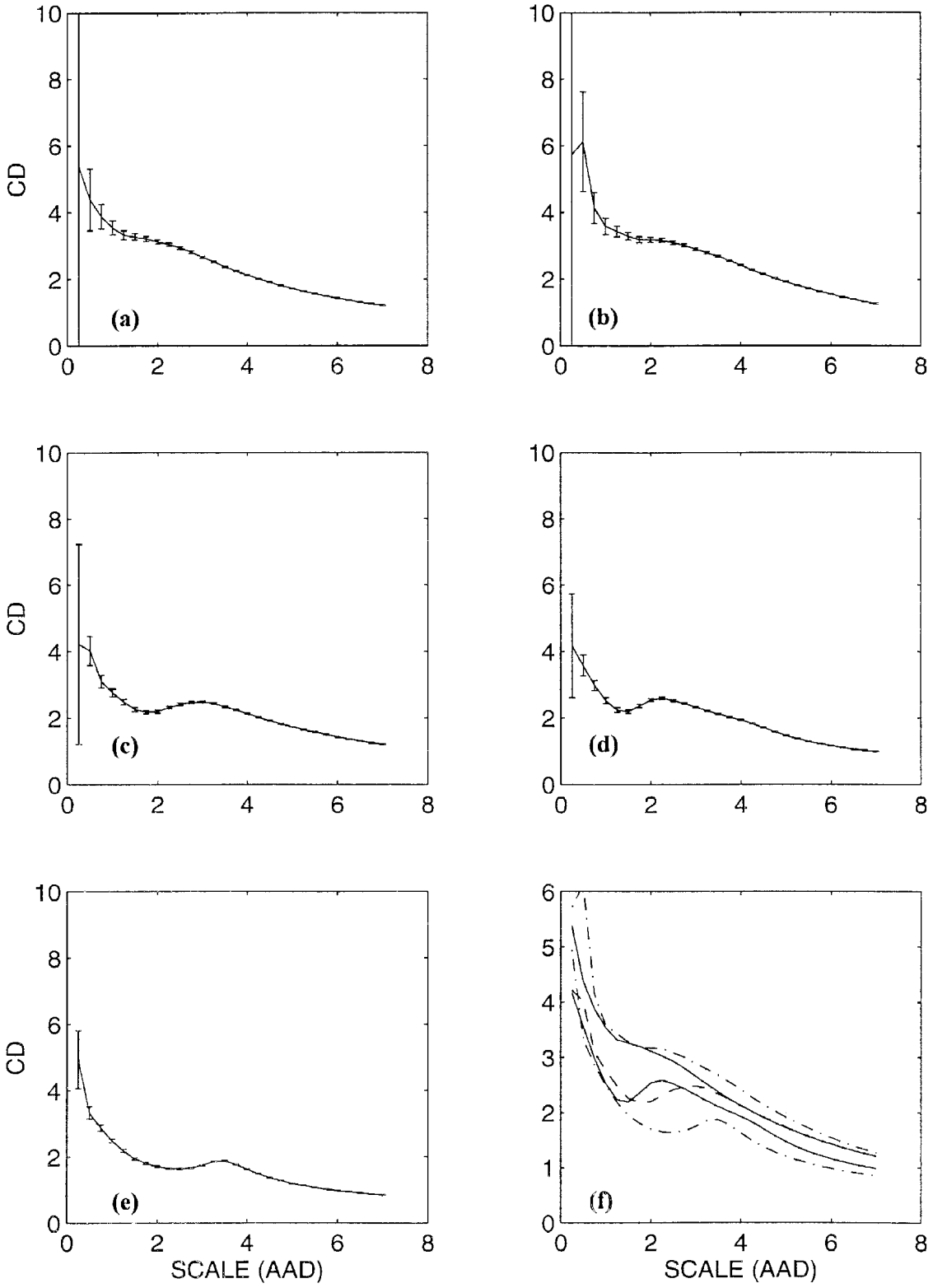

Fig. 4.7. Correlation dimension spectrum of the power P for (a) 75 rpm, (b) 100 rpm (dataset #091802), (c) 100 rpm (dataset #091803), (d) 125 rpm, (e) 150 rpm, (f) composite.

Figures 4.8–4.9 show period-1 (m=1) return maps for E_i^+ and E_i^- (i.e., E_{i+1}^+ vs E_i^+, and E_{i+1} vs E_i^-, respectively). These figures show the structure of regions that are visited by the tool-part motion, and regions that are not visited at all. The dynamics are clustered around the diagonal, $E_{i+1} = E_i$ in both figures, which corresponds to an unstable period-1 orbit. This structure is significantly different from the discrete clusters in the return map for negative- and positive-starting return times for the accelerations, as shown in Figs. 4.11–4.16 of Ref. 1.

Figure 4.8 shows return maps for E_i^+ (E_{i+1}^+ vs E_i^+) that change in structure with increasing spindle speed. The nonchatter return map in Fig. 4.8(a) is most complex (two sharp corners and two fingers in the cluster) with the least variability (most compact) at a spindle speed of 75 rpm. Figure 4.8(b) shows the nonchatter return map at 100 rpm which is less complex (two rounded corners and two fingers in the cluster). Figure 4.8(c) shows a nonchatter return map for dataset #091803 (also at 100 rpm but with a slightly smaller workpiece radius) with two distinct clusters, one on each side of the diagonal. Figure 4.8(d) has a single, somewhat elongated cluster at 125 rpm (chatter) with significantly more variability than the nonchatter dynamics. Figure 4.8(e) also has one high-variability cluster at 150 rpm (chatter). The clear progression is from more to less complexity and from less to more variability, corresponding to a weakening in chaotic features and larger variability in cycle-to-cycle energy as the spindle speed increases.

Figure 4.9 also shows return maps for E_i^- (E_{i+1}^- vs E_i^-) with large changes in structure as spindle speed increases. The three nonchatter return maps at 75–100 rpm [Figs. 4.9(a)–4.9(c)] have three or four arms and resemble various perspectives of a bird in flight. The return map at 125 rpm [Fig. 4.9(d)] is a more compact cluster with somewhat less variability (corresponding to periodic chatter motion) and short, diffuse arms (corresponding to some variability). The return map at 150 rpm [Fig. 4.9(e)] shows an even more compact cluster (corresponding to very strong periodic chatter motion) with three very diffuse arms (indicating little chaotic variability). The progression is again from more to less complexity, and from less to more periodicity, as the spindle speed rises. Moreover, these return maps for E_i^- are very different from the return maps for E_i^+ (Fig. 4.8) because the workpiece constrains the tool motion in the negative direction but not in the positive direction. We focus subsequent analysis on return maps for E_i^-, which show favored directions more clearly as indications of the (un)stable manifolds.

Based on work by Schiff et al. [29], we use the following criteria to determine a fixed point, together with (un)stable directions to and from the fixed point:

(1) points approach the unstable fixed point along a locally linear stable direction;
(2) points depart from the unstable fixed point along a locally linear unstable direction; and
(3) repeated approaches to and departures from the same fixed point occur along the same directions.

These three criteria provide a statistical basis of multiple approaches to and departures from the fixed point(s) and also avoid nonphysical identifications from isolated (random) events. For this purpose, we find ten or more E_i^- points that satisfy $| E_i^- - E_{i+m}^- | \leq \epsilon$, for the chosen period-m motion. We measure ϵ in units of the absolute average deviation (AAD). Referring to Eq. 4.1 for AAD, x_i in this instance is E_i^-, and $\underline{x}$ is the average over E_i^-. We analyze E_i^+ similarly. Subsequent discussion presents specific results of our analysis.

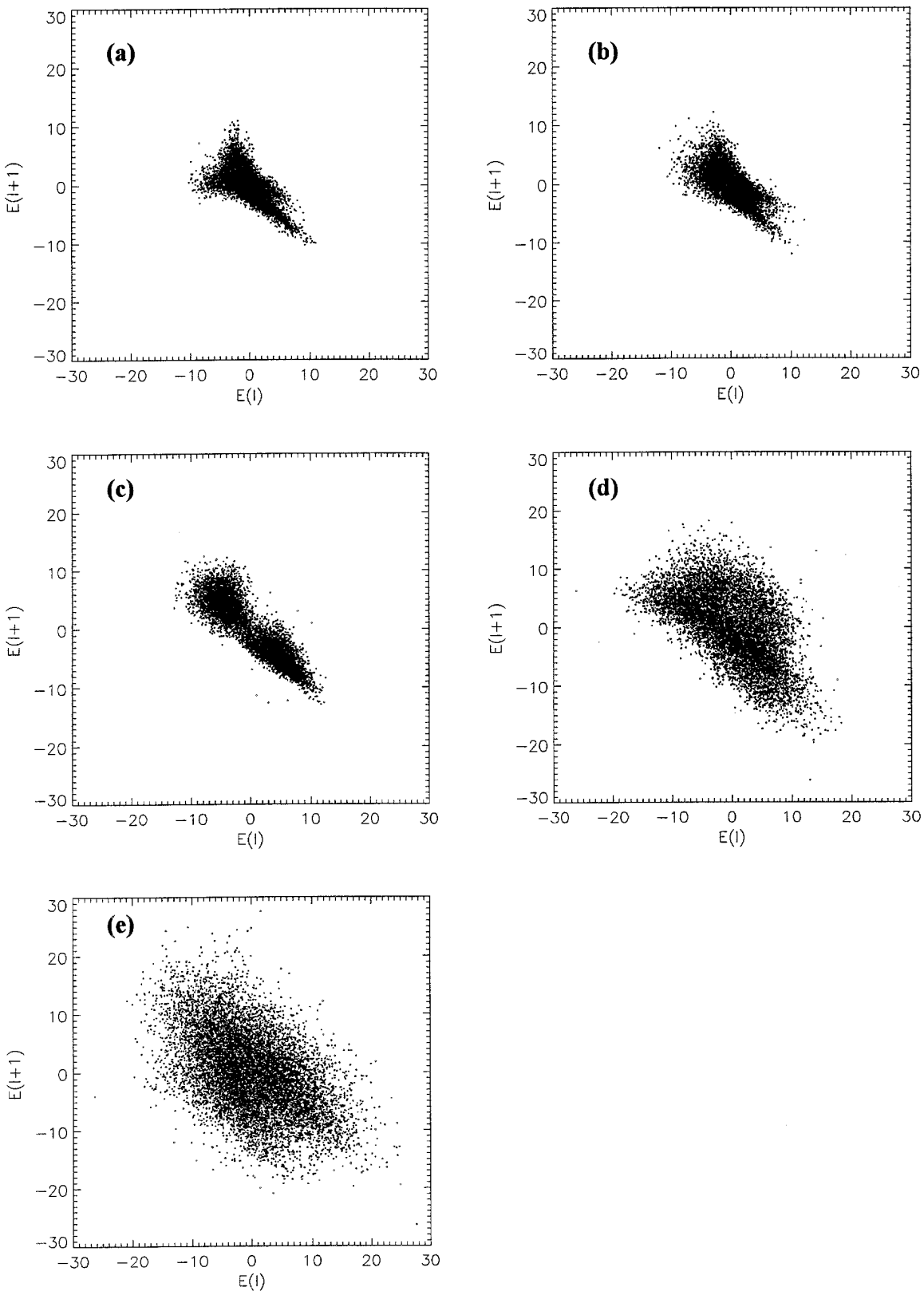

Fig. 4.8. Return maps for E_i^+ (lag = 1): (a) 75 rpm, (b) 100 rpm (dataset #091802), (c) 100 rpm (dataset #091803), (d) 125 rpm, (e) 150 rpm.

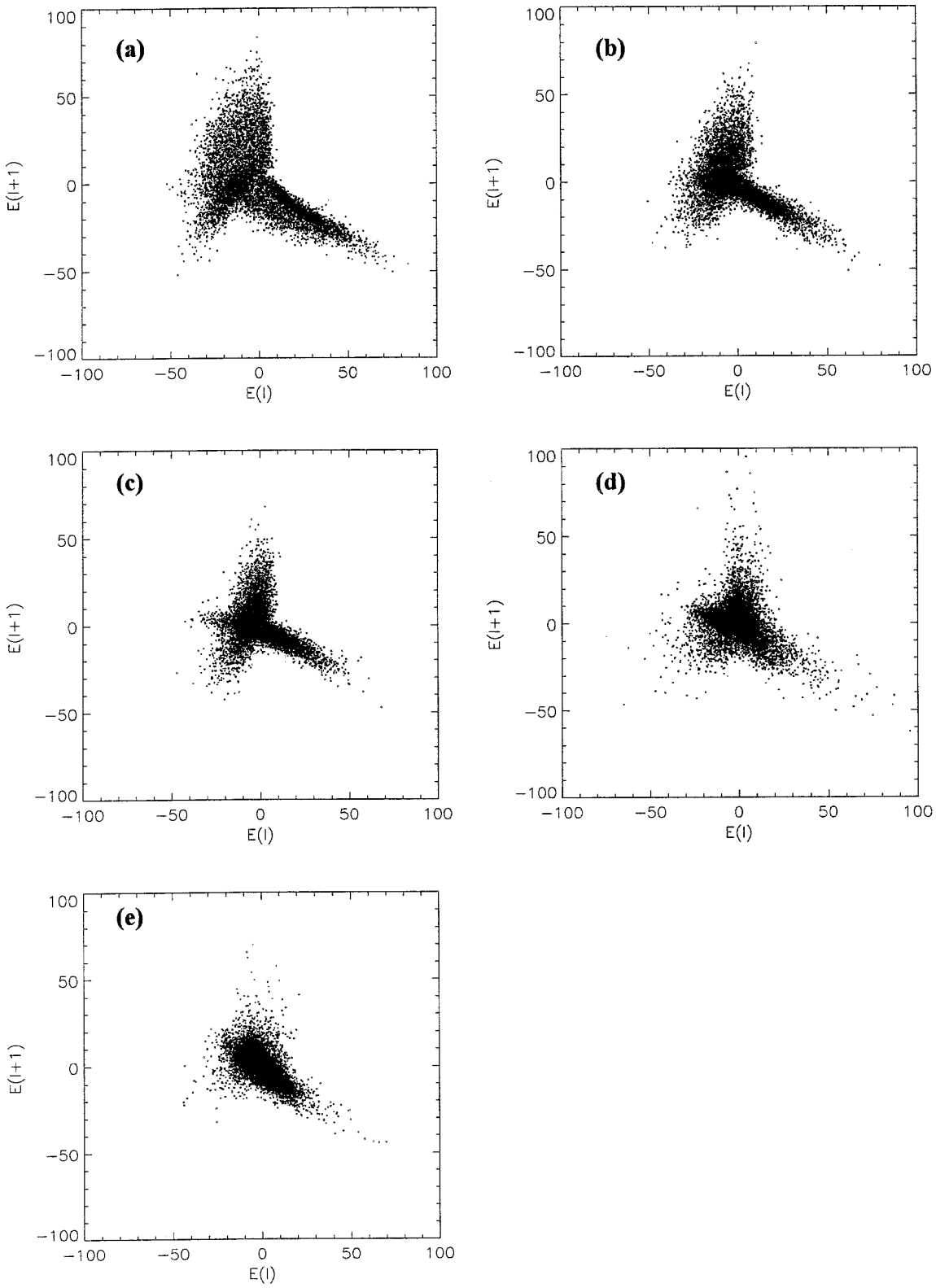

Fig. 4.9. Return maps for E_i^- (lag = 1): (a) 75 rpm, (b) 100 rpm (dataset #091802), (c) 100 rpm (dataset #091803), (d) 125 rpm, (e) 150 rpm.

Figure 4.10 shows return maps of E_i^- for dataset #091801 (nonchatter turning at 75 rpm). These figures show E_{i+1+n}^- vs E_{i+n}^-, for $-5 \le n \le 5$, where the i-values correspond to points that lie near the period-1 fixed point with $(E_{i+1}^-)^2 + (E_i^-)^2 \le \epsilon^2$, for $\epsilon = 0.2$ AAD. Figure 4.10(f) shows the fixed point as a small, circular cluster of points, centered on the origin. The figures start with the fifth precursor to the fixed point (n = –5) in Fig. 4.10(a), then the fourth precursor (n = –4) in Fig. 4.10(b),..., the fourth successor to the fixed point (n = +4) in Fig. 4.10(j), and finally the fifth successor cluster (n = +5) in Fig. 4.10(k). These figures show the evolution of the machining dynamics toward, near, and away from this period-1 fixed point.

We next examine the details of this return map. Figure 4.10(g) shows points immediately after the fixed point (i.e., n = +1). This cluster has a vertical orientation because most points leave the fixed-point region in a <u>single</u> step; this single-step departure occurs in all five datasets. This feature is in sharp contrast to most dynamical systems, which require two (or more) steps for a return map point to leave the neighborhood of the fixed point. In the subsequent step [Fig. 4.10(h) with n = +2], most of the points (forming a dense mass of points in this and other subplots) occur on a straight line that has a negative slope and magnitude less than one, indicating the stable direction. In the next step [Fig. 4.10(i) with n = +3], the massive cluster of points lies along a roughly straight line with positive slope and magnitude greater than one, corresponding to the unstable direction. In subsequent steps [Figs. 4.10(j)–(k)], the massive cluster alternates between following the same stable and unstable directions. The remaining seven points in the cluster occur very close to the fixed point in Fig. 4.10(g) and in the next step [Fig. 4.10(h)] follow the same vertical straight line along which previous mass of points departed from the fixed point. In subsequent frames [Figs. 4.10(i)–(k)], these seven points also alternate between the same stable and unstable directions that the massive cluster of points followed. The points also follow the same alternation between the (un)stable directions in approaching the fixed point [Figs. 4.10(a)–(d)]. Thus, the vertical direction in Figs. 4.10(g)–(h) and the horizontal direction in Fig. 4.10(e) are artifacts of the return map construction and do not show the real (un)stable direction(s) because the return map points arrive at and depart from the fixed-point region in one step. Figure 4.10(l) is a composite plot of the stable and unstable directions.

Figure 4.11 shows composite plots of the (un)stable directions from the above analysis. Figure 4.11(a) shows the (un)stable directions (manifolds) from the composite plot in Fig. 4.10(l) as large dots for dataset #091801. For reference, Fig. 4.11(a) also shows all of the other return map points (small dots) from Fig. 4.9(a), illustrating how the (un)stable direction(s) occur within the complete return map. In the same fashion, Figs. 4.11(b)–(e) show composite plots of the (un)stable directions for datasets #091802–091805, respectively. We note that the (un)stable directions are only a portion of the complete return map in Fig. 4.11(a) because the machining dynamics is far from chatter at 75 rpm. However, the (un)stable manifolds engulf the return map attractors in Figs. 4.11(b)–(e) because the tool-part motion is close to or in chatter, and, thus, the dynamics spend most of the time moving near the fixed point. Moreover, Figs. 4.11(d)–(e) show very little of the unstable manifold (the direction with positive slope and a magnitude greater than one), because chatter involves motion mostly toward and at the fixed point and seldom away from the fixed point. We confirmed these (un)stable manifolds (not shown) for other search radii (ϵ), and by requiring that the dynamics remain within this radius of the fixed point for two and three steps in the return map. The dominant motion is near the fixed point during chatter, consistent with our earlier interpretation of tool chatter as periodic motion near the fixed point [1].

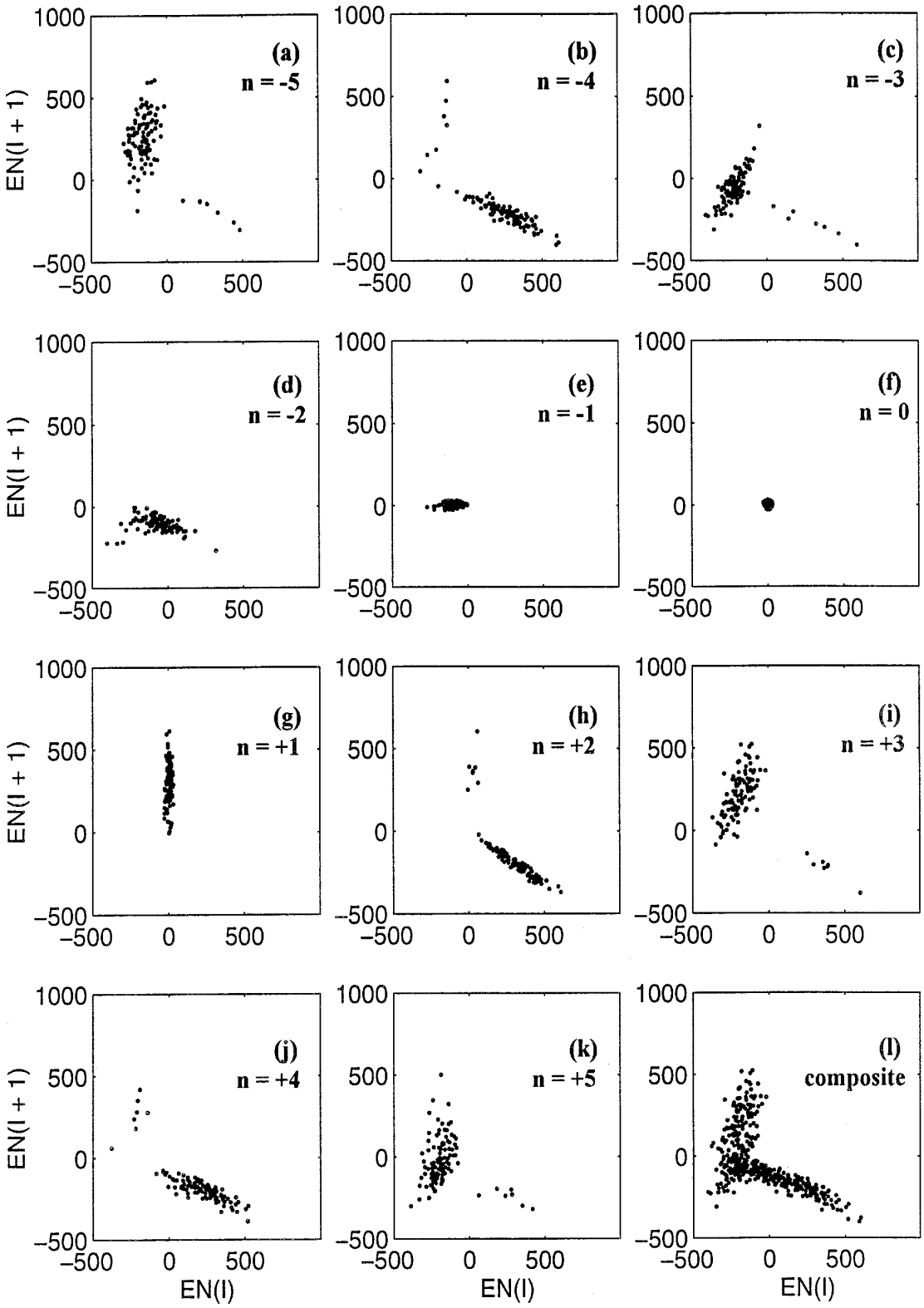

Fig. 4.10. Return maps for E_i^- (lag = 1) to and from the fixed point for dataset #091801 (see text for discussion).

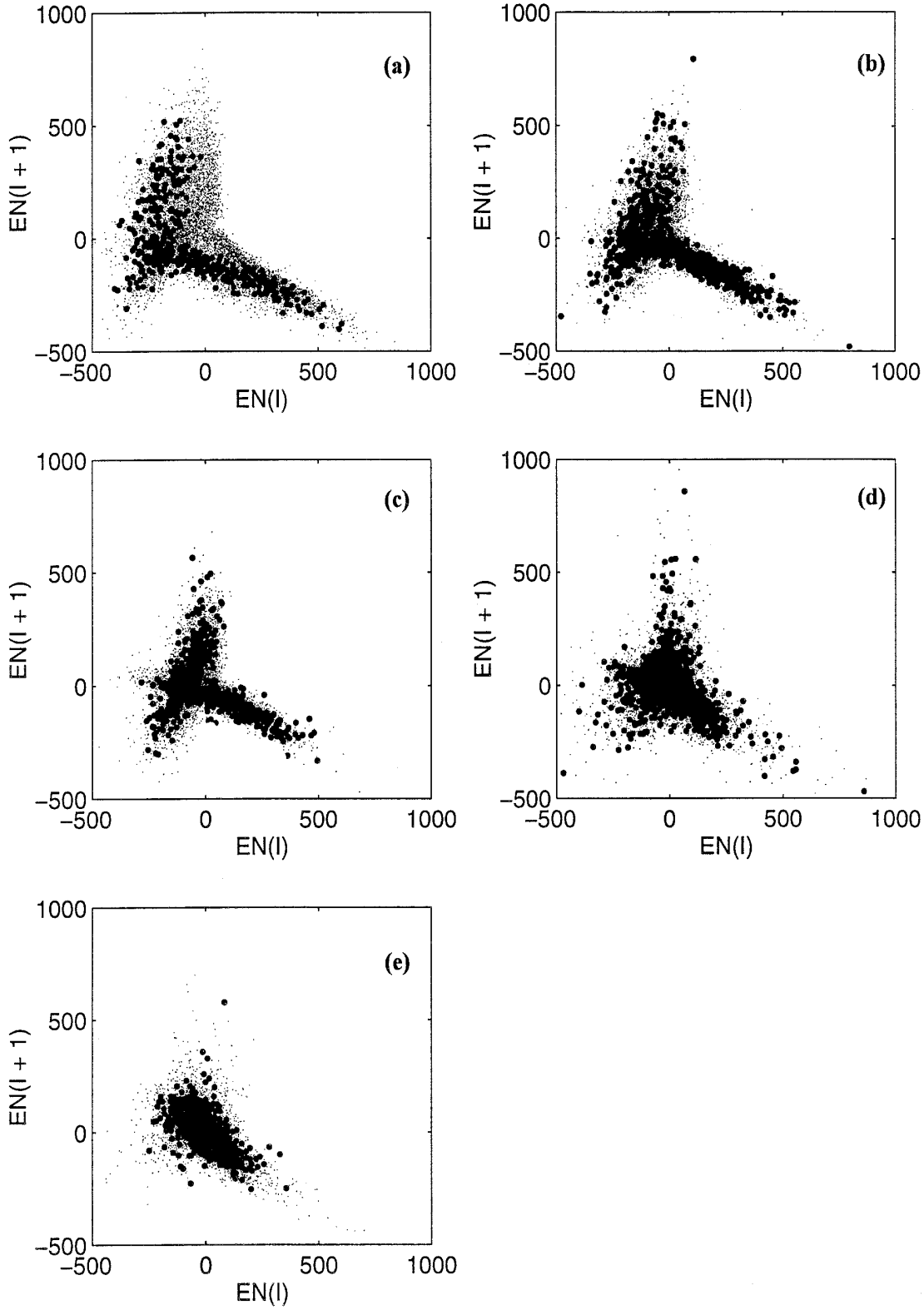

Fig. 4.11. Stable and unstable manifolds for E_i^- (lag = 1): (a) 75 rpm, (b) 100 rpm (dataset #091802), (c) 100 rpm (dataset #091803), (d) 125 rpm, (e) 150 rpm.

Figure 4.12 shows an example of period-1 E_i^+ return maps for dataset #091801 (75 rpm in nonchatter) analogous to Fig. 4.10. The residence time at the fixed point is three timesteps [Figs. 4.12(e)–4.12(g)] with ϵ = 0.6 AAD. The slope of the incoming direction decreases monotonically in Figs. 4.12(a)–4.12(d), with values ~2, ~1, ~1/2, and ~0, respectively. The magnitude of the slope of the outgoing direction also decreases monotonically in Figs. 4.12(h)–4.12(k), with values ~4, ~2, ~1, and ~1/2. For all spindle speeds, we obtained similar results which violate the statistical criteria for unstable fixed points and (un)stable manifolds. Consequently, the composite return maps have no clear directionality, but are elongated blobs that resemble fuzzy versions of the original return maps in Fig. 4.8. Thus, we did not study E_i^+ return maps further.

The return maps for E_i^- and E_i^+ are very different because the tool motion is constrained in one sign of each acceleration direction by contact with the workpiece, but is unconstrained in the other sign (see Fig. 2.1). For example, Fig. 2.9 of Ref. 1 shows a clear limit in the x-component of acceleration ($A_x \gtrsim$ -100 in. AU) at all four spindle speeds, but no such constraint exists for $A_x > 0$. Moreover, (constrained) valleys for $A_x < 0$ are much flatter, while the (unconstrained) peaks for $A_x > 0$ have sharp changes. The waveform for A_x is asymmetric because cutting occurs in the negative-x direction, resulting in chip removal as a dissipative, discontinuous process. Motion for $A_x > 0$ does not involve cutting and, thus, is conservative and continuous. Analogous arguments for A_y and A_z (Figs. 2.10–2.11 in Ref. 1) lead to the above conclusion.

We investigated higher-period fixed points. Figure 4.13 shows the occurrence frequency of period-m motion relative to the dominant occurrence frequency. The left (right) column of subplots in Fig. 4.13 show the period-m occurrence frequency relative to period-1 for positive- (negative-) going energies, respectively. The results for successive datasets #091801–091805 progress from the top to the bottom plots, respectively. This plot shows the occurrence of E_i^+ pairs and E_i^- pairs that satisfy the condition, $(E_{i+m}^{\pm})^2 + (E_i^{\pm})^2 \leq \epsilon^2$, for ϵ = 0.5 AAD. For period-m motion, we also excluded pairs that had E_i values in period-1 through period-(m-1) to avoid multiple counting of the periodicities. Period-1 dominates in all but one case. Period-2 dominates in E_i^+ for dataset #091803 [Fig. 4.13(e)] and also is evident in Fig. 4.8(c) as the two-lobed structure on either side of the diagonal ($E_{i+1}^+ = E_i^+$). The period-2 features are related to the transition from nonchatter to chatter cutting as the spindle speed increases from 100 to 125 rpm. We further note that the subdominant peaks in the occurrence distributions for $E_i^{\pm}$ [Figs. 4.13(a)–4.13(f)] correspond to other periodicities that contribute to the chaotic motion in nonchatter turning. Figures 4.13(h) and 4.13(j) show no subdominant peaks, corresponding to the overwhelming presence of period-1 dynamics during chatter. We did not pursue further details of period-m motion due to the predominance of period-1 dynamics in $E_i^{\pm}$

We also studied return maps for cycle times, $T_i^{\pm} = t_{i+1}^{\pm} - t_i^{\pm}$. We give cycle time values in timesteps with 2×10^{-5} seconds per timestep from a data sampling rate of 50,000 Hz. Figure 4.14 shows the period-1 return map (T_{i+1}^+ vs T_i^+) for each dataset. Figure 4.14(a) (nonchatter at 75 rpm) shows a large cluster centered on the diagonal, $T_{i+1}^+ = T_i^+ = 20$. Other discrete clusters occur on either side of the diagonal with values of $T_i^+ \sim 2$, $T_i^+ \sim 30$, and $T_i^+ \sim 60$. Figures 4.14(b)–4.14(c) (nonchatter at 100 rpm) show the same (but smaller) cluster that is centered at and 150 rpm, respectively) have a single dense cluster that is centered on the diagonal at $T_{i+1}^+ = T_i^+ = 15$. Variation in cycle times is large at 75 rpm ($1 < T_i^+ < 65$), smaller at 100 rpm ($2 < T_i^+ <$ 32 for dataset #091802 and $6 < T_i^+ < 25$ for dataset #091803), smaller still at 125 rpm ($6 < T_i^+ <$

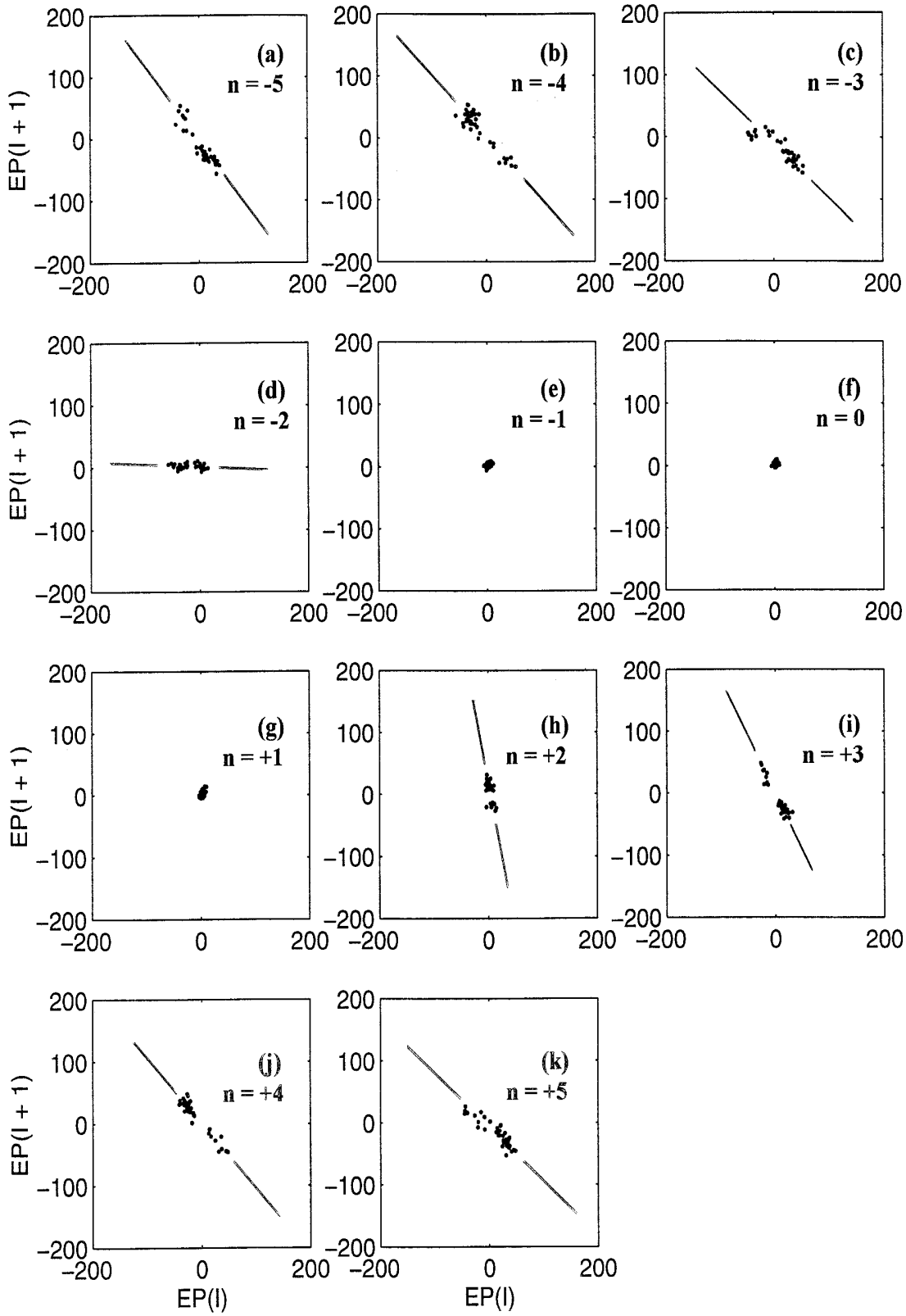

Fig. 4.12. Period-1 return map for E_i^+ for dataset #091801 (see text for discussion).

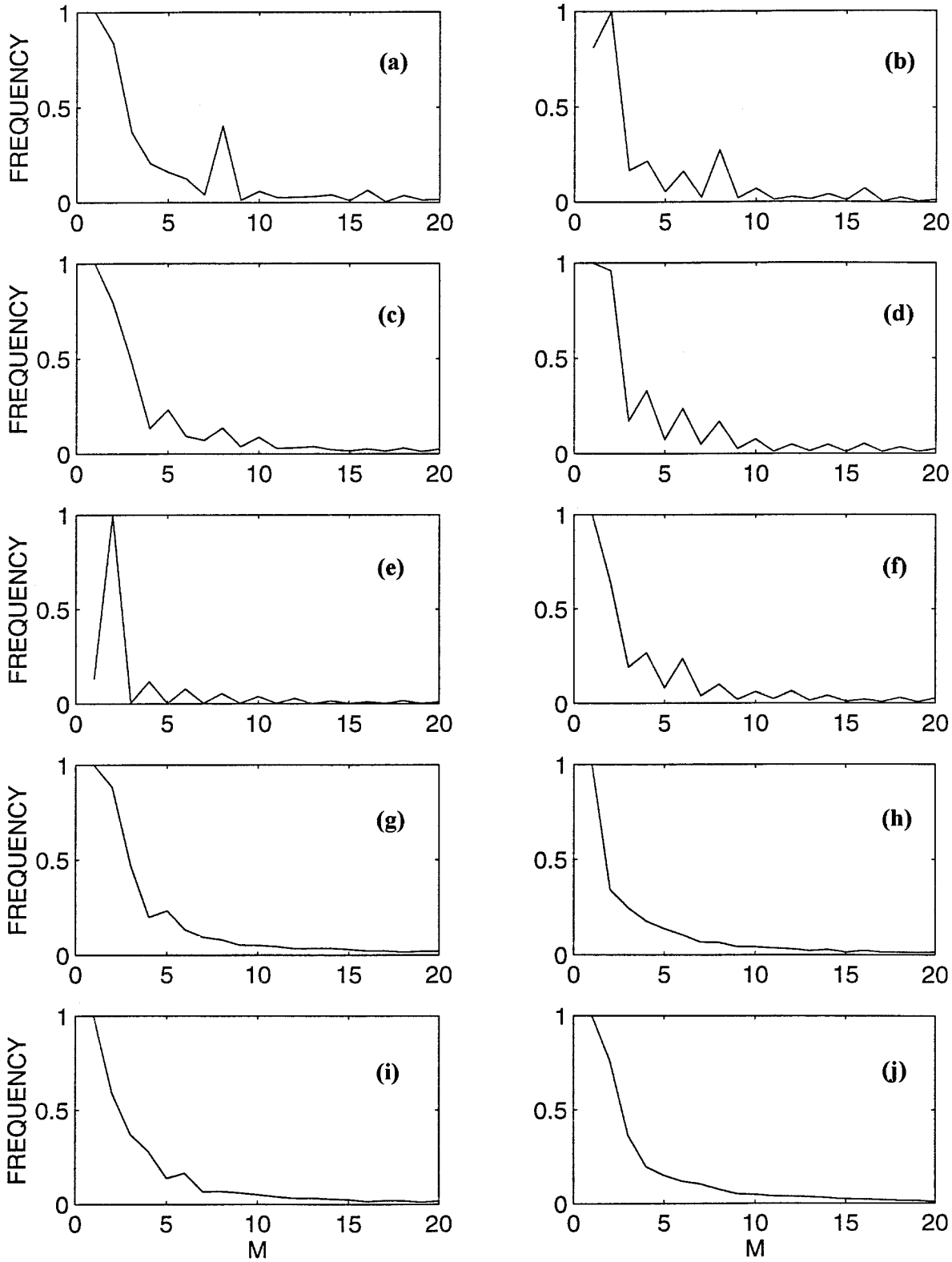

Fig. 4.13. Normalized period-m occurrence frequency vs m for E_i^+ (left column) and E_i^- (right column) for datasets #091801 (top)–091805 (bottom).

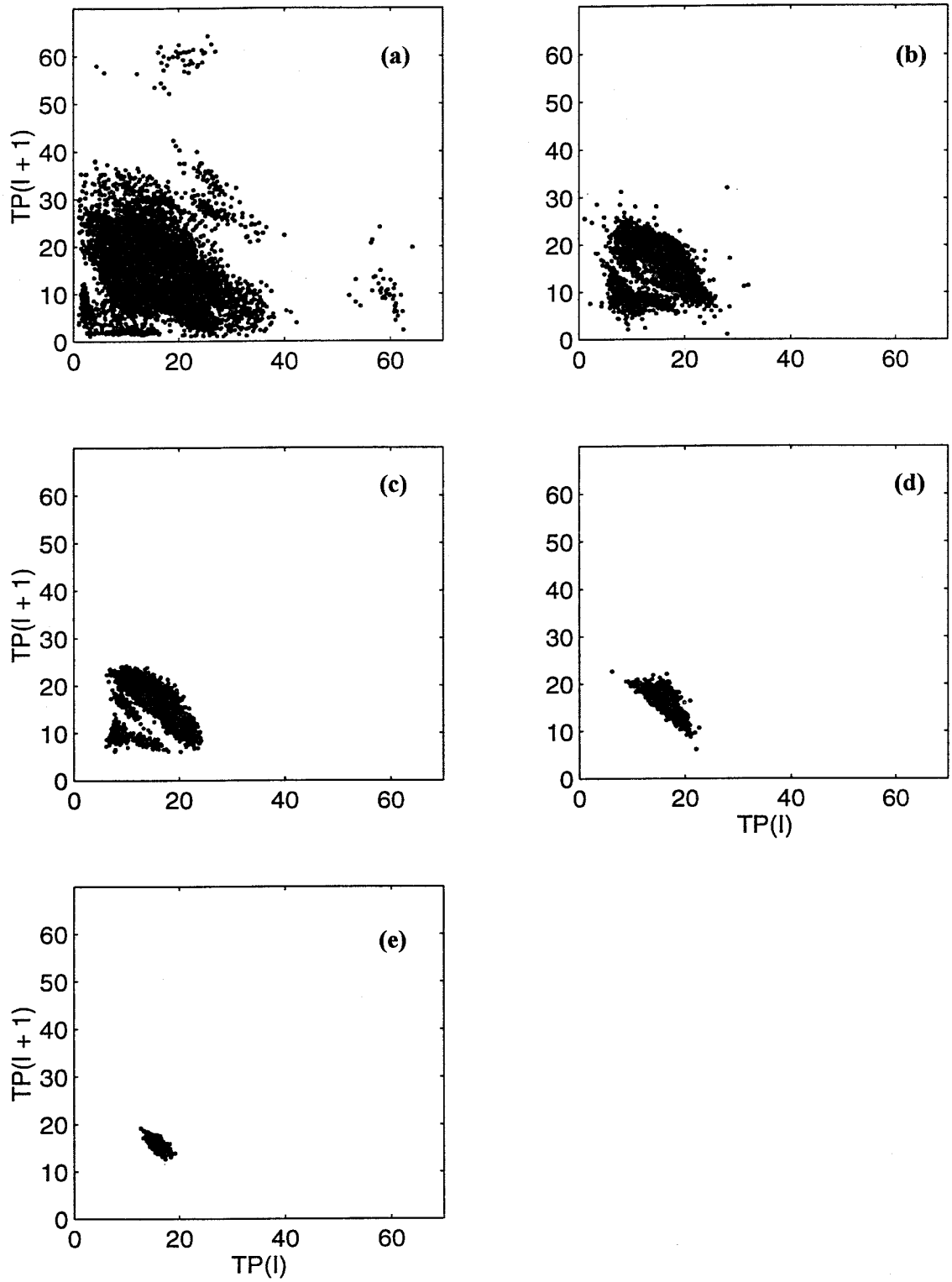

Fig. 4.14. Period-1 return maps for T_i^+: (a) 75 rpm, (b) 100 rpm (dataset #091802), (c) 100 rpm (dataset #091803), (d) 125 rpm, (e) 150 rpm.

23), and smallest at 150 rpm ($12 < T_i^+ < 20$). This trend is consistent with many periodicities for chaotic (nonchatter) cutting and a single dominant periodicity for chatter. In every instance, the clusters lie perpendicular to the diagonal, suggesting the presence of many periodicities.

Figure 4.15 shows the period-2 T_i^+ return maps (T_{i+2}^+ vs T_i^+), with the same organization as in Fig. 4.14. Figure 4.15(a) (nonchatter at 75 rpm) shows a large cluster that is centered on the diagonal at $T_{i+2}^+ = T_i^+ = 15$ with two diffuse arms along the lines of $T_i^+ = 20$ and $T_{i+2}^+ = 20$. Three other small clusters appear in Fig. 4.15(a) at $T_i^+ \sim 5$, $T_i^+ \sim 30$, and $T_i^+ \sim 60$. Figures 4.15(b)–4.15(c) (nonchatter at 100 rpm) show a single massive cluster with small arms along the lines of $T_i^+ = 10$ and $T_{i+2}^+ = 10$. Figures 4.15(d)–4.15(e) (125 and 150 rpm during chatter, respectively) show one cluster on the diagonal, centered at $T_{i+2}^+ = T_i^+ = 15$. The cluster variability is the same as in Fig. 4.14. The clusters are oriented along the diagonal, especially for Figs. 4.15(b)–4.15(e).

Figure 4.16 shows the period-3 T_i^+ return map (T_{i+3}^+ vs T_i^+), with the same organization as in Fig. 4.14. Figure 4.16(a) has an elongated cluster that is centered on the diagonal at $T_{i+3}^+ = T_i^+ = 15$, plus four arms, as well as some smaller diffuse clusters. Figures 4.16(b)–4.16(d) show circular clusters that are all centered on the diagonal at $T_{i+3}^+ = T_i^+ = 15$.

Figure 4.17 shows period-1 T_i^- return maps (T_{i+1}^- vs T_i^-), with the same organization as in Fig. 4.14. Many clusters occur at all spindle speeds with decreasing complexity as spindle speed increases. The clusters have a reflection symmetry about the diagonal. Cluster spacing is more regular in chatter [Figs. 4.17(d)–4.17(e)]. The complexity decrease with increasing spindle speed is consistent with nonchatter chaos and strong periodicity (weak chaos) during chatter.

Figure 4.18 shows period-2 T_i^- return maps (T_{i+2}^- vs T_i^-) with the same organization as in Fig. 4.14. Many discrete clusters occur at all spindle speeds, with high cluster complexity during nonchatter cutting [Figs. 4.18(a)–4.18(c)] and less complexity during chatter [Figs. 4.18(d)–4.18(e)]. These (and higher period) clusters have a more regular spacing than in Fig. 4.17.

Figure 4.19 displays the relative occurrence frequency distribution for $T_i^\pm$, using the same methodology as in Fig 4.13. Period-1 motion is dominant in nonchatter cutting [Figs. 4.19(a)–4.19(d) and 4.19(f)]. Period-2 dominates in near-chatter [Fig. 4.18(e)] and chatter cutting [Figs. 4.19(g)–4.19(j)]. We did not pursue higher-period return maps further.

We finally analyze return maps for T_i^+ because the discrete, regular structure in T_i^- return maps (Figs. 4.17–4.18) is not suggestive of (un)stable manifolds. Figure 4.20 shows an example for dataset #091802 (100 rpm in nonchatter) analogous to Figs. 4.10 and 4.12. The residence time at the fixed point is three timesteps [Figs. 4.20(e)–4.20(g)] with $\epsilon = 0.6$ AAD. The magnitude of the slope of the incoming and outgoing directions decreases monotonically [Figs. 4.20(a)–4.20(d)] of the slope of the incoming and outgoing directions decreases monotonically [Figs. 4.20(a)–4.20(d) and 4.20(h)–4.20(k)] as the dynamics arrive at and depart from the fixed point. For all spindle speeds, we obtained similar results which violate the statistical criteria for unstable fixed points and (un)stable manifolds. Consequently, the composite return maps have no clear directionality (not shown) but are simply elongated blobs that resemble fuzzy versions of the original return maps in Fig. 4.8. Thus, we did not study T_i^+ return maps further.

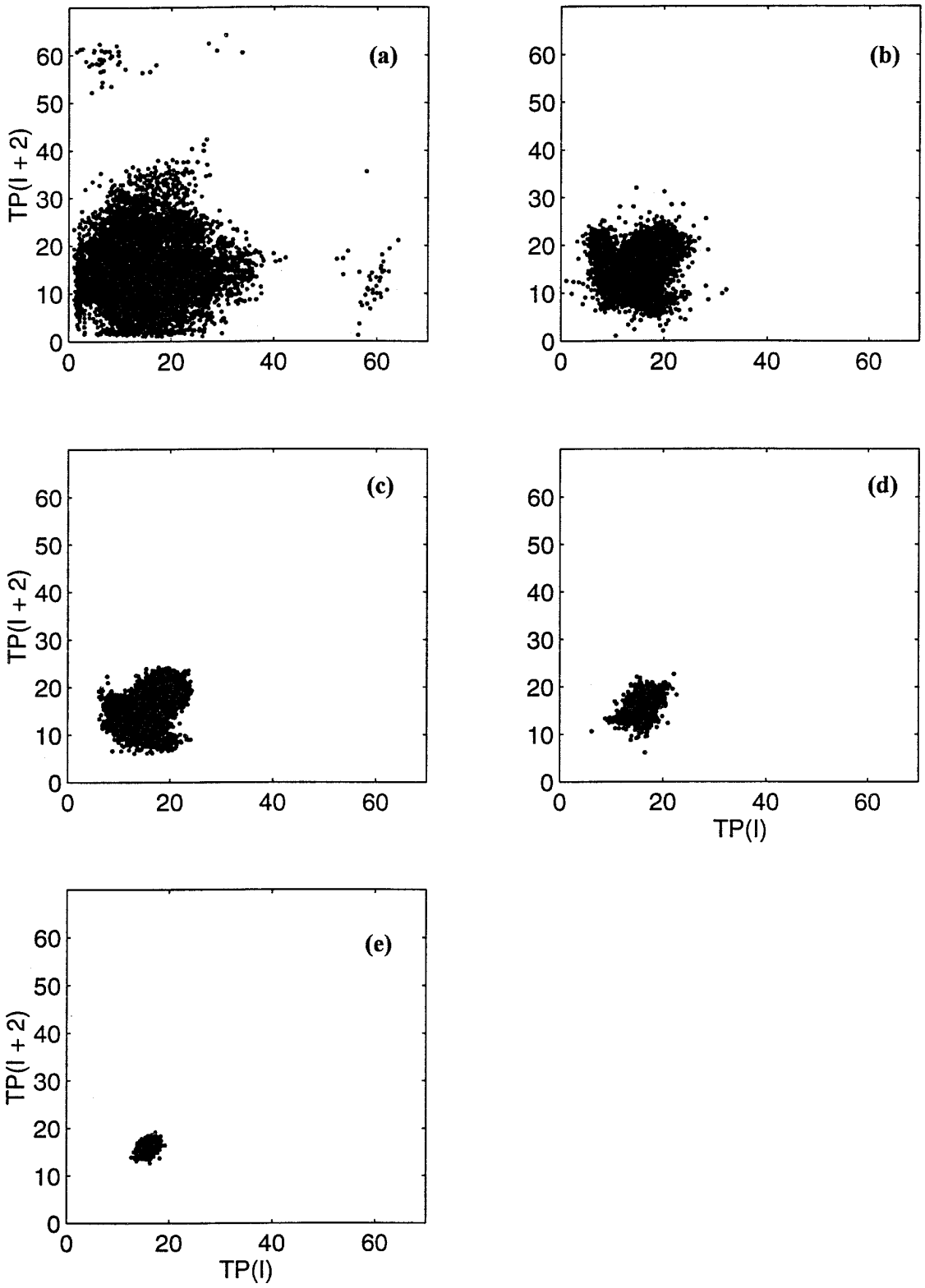

Fig. 4.15. Period-2 return maps for T_i^+: (a) 75 rpm, (b) 100 rpm (dataset #091802), (c) 100 rpm (dataset #091803), (d) 125 rpm, (e) 150 rpm.

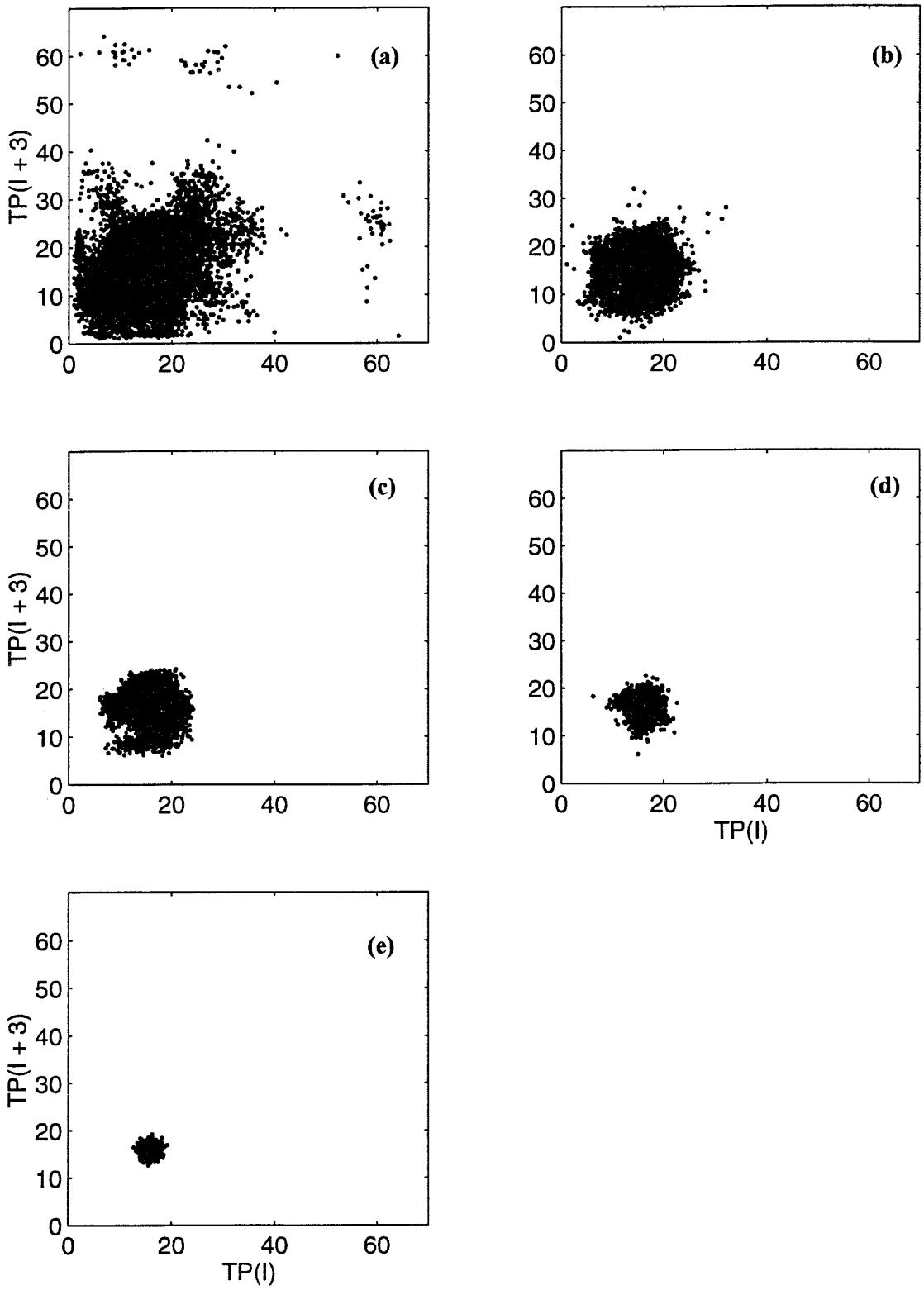

Fig. 4.16. Period-3 return maps for T_i^+: (a) 75 rpm, (b) 100 rpm (dataset #091802), (c) 100 rpm (dataset #091803), (d) 125 rpm, (e) 150 rpm.

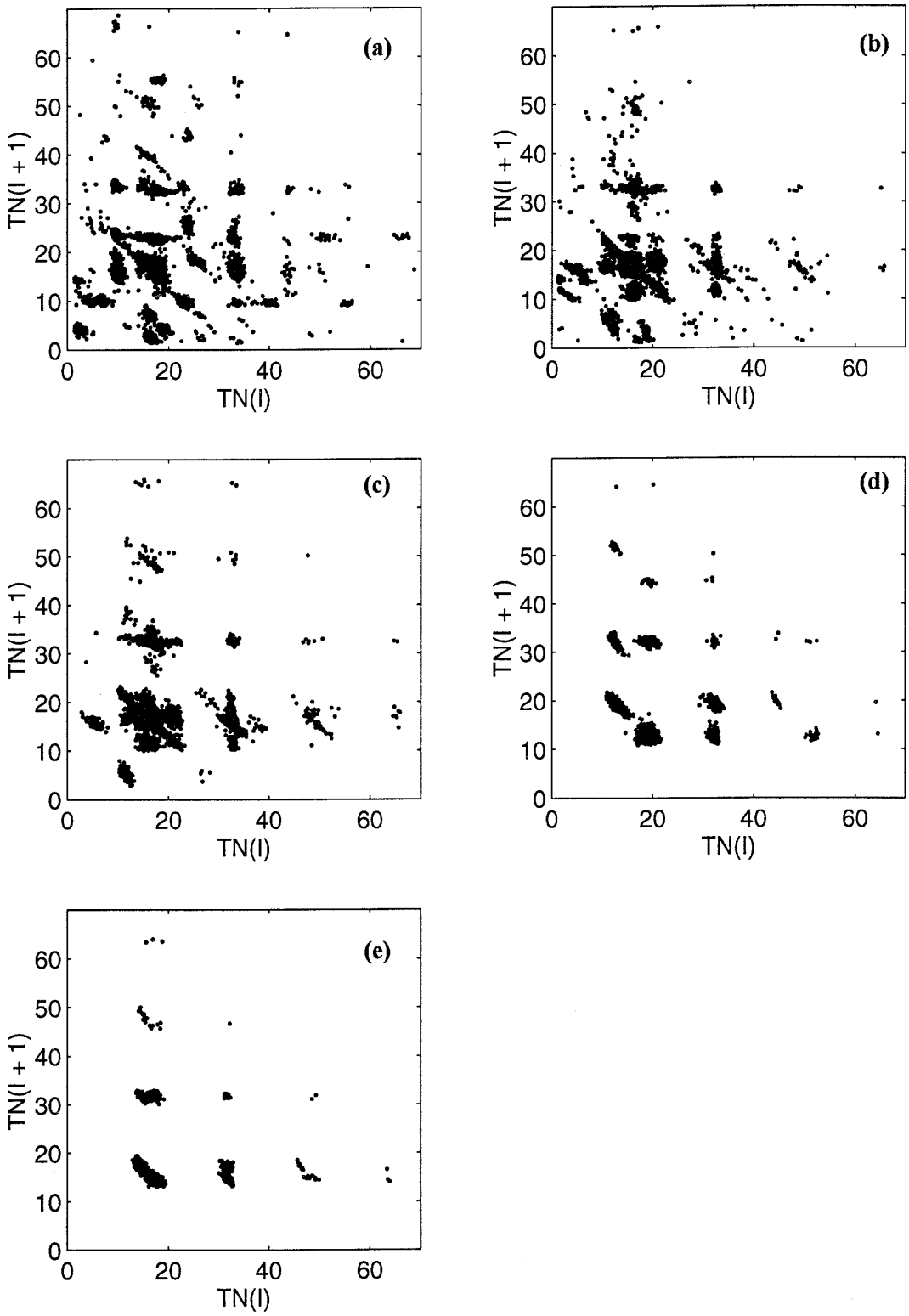

Fig. 4.17. Period-1 return maps for T_i^-: (a) 75 rpm, (b) 100 rpm (dataset #091802) (c) 100 rpm (dataset #091803, (d) 125 rpm, (e) 150 rpm.

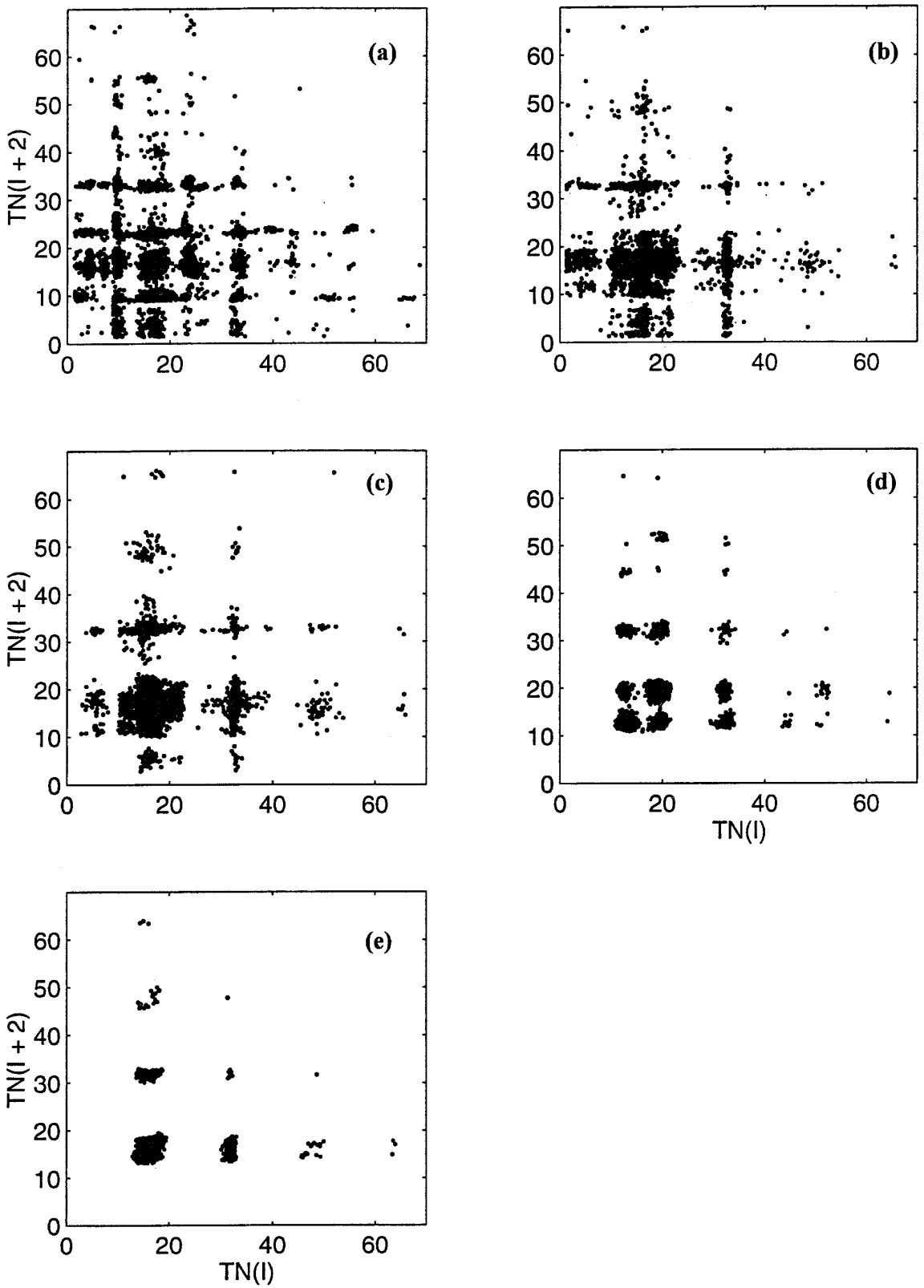

Fig. 4.18. Period-2 return maps for T_i^-: (a) 75 rpm, (b) 100 rpm (dataset #091802), (c) 100 rpm (dataset #091803), (d) 125 rpm, (e) 150 rpm.

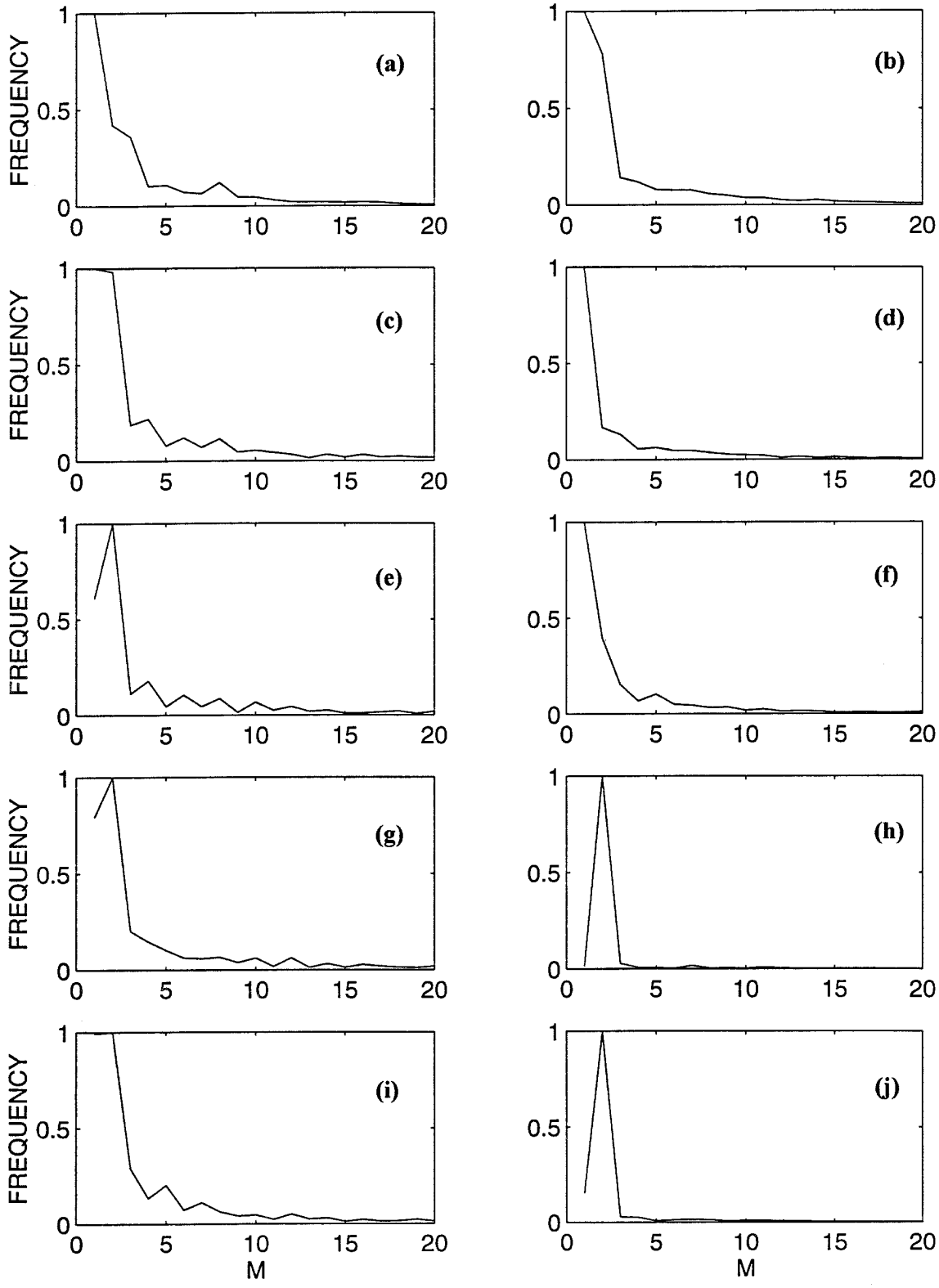

Fig. 4.19. Normalized period-m occurrence frequency vs m for T_i^+ (left column) and T_i^- (right column) for datasets #091801 (top)–091805 (bottom).

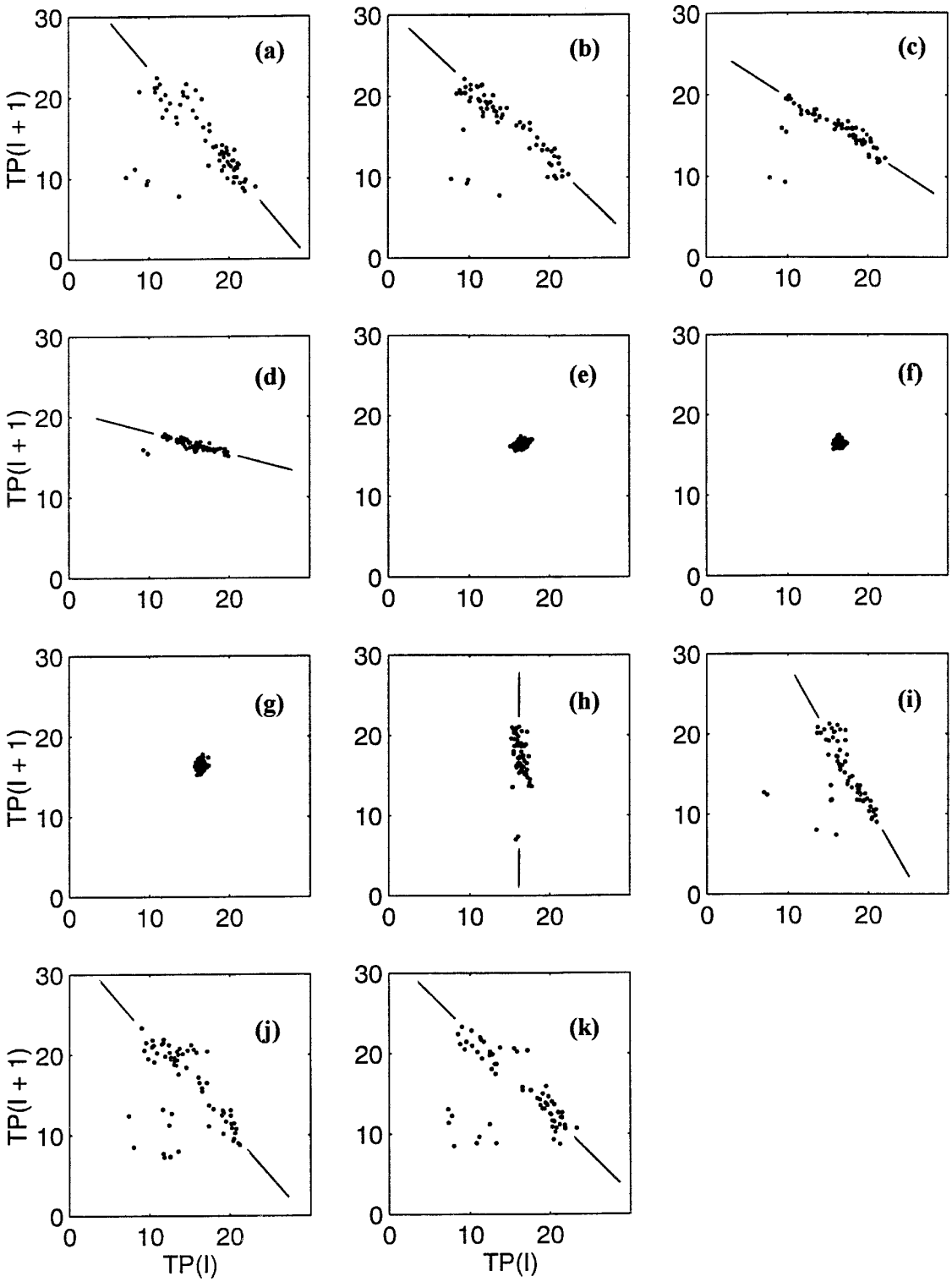

Fig. 4.20. Period-1 return map for T_i^+ to and from the fixed point for dataset #091802 (see text for discussion).

5. DISCUSSION

In this paper, we explore the prospects of controlling machine tool chatter by using the OGY scheme for chaos maintenance. We find that the tool-part dynamics are best revealed in the sequence of negative-starting cycle energies (E_i^-), including a detailed analysis of return maps for E_i^-. This analysis reveals the following features:

- period-1 motion totally dominates the turning dynamics with and without chatter;
- nonchatter cutting displays (un)stable manifolds in the energy return map, along which the dynamics move toward and away from the period-1 fixed point;
- chatter displays a period-1 fixed point, a clear stable manifold, and a small unstable manifold, arising from dynamics that seldom move away from the fixed point;
- return maps reveal dynamics that depart from and arrive at the period-1 fixed point in a single step rather than in several steps as in most chaotic processes; and
- many periodicities exist, combining to create chaotic features, especially in nonchatter.

These findings have implications for the pursuit of experimental approaches to chatter control by using the OGY scheme. Indeed, chatter control seems possible in principle, either via maintenance of the chaotic (nonchatter) dynamics, or by conversion of periodic motion (chatter) to chaotic (nonchatter) dynamics. Based on the results of the present analysis, the prospects for chatter control by chaos maintenance are rather poor, due to the single-step departure from the period-1 neighborhood (e.g., Fig. 4.10). Conversion of periodic (chatter) dynamics to more chaotic (nonchatter) motion is one option via dynamic damping, based on recent work by Pratt and Nayfeh [57–58]. However, we are pursuing a new alternative [60-61], based a phase-space (PS) representation of time series data, which in turn is converted into a probability density function. An advanced version of this technique [62] connects sequential pairs of points in the PS, thereby providing a data-driven representation of multidimensional flow. We plan to use this approach to identify noisy transitions between convergent (folding) and divergent (stretching) dynamics. Extreme sensitivity to perturbations at one (or more) of these transition points would, in principle, allow robust control of tool chatter.

ACKNOWLEDGMENTS

We thank R. F. Holdaway and M. A. Akerman for their valuable comments on our work. We also gratefully acknowledge the encouragement and programmatic support of this work by S. C. Robinson and T. L. Williams. This research was sponsored by the U.S. Department of Energy, Office of Defense Programs, under CRADA #Y1295-0357. V. A. Protopopescu was partly supported by the Office of Energy Research in the U.S. Department of Energy. The work was performed at the Oak Ridge National Laboratory, which is managed by the Lockheed Martin Energy Research Corporation for the U.S. Department of Energy, under Contract No. DE-AC05-96OR22464.

REFERENCES

1. L. M. Hively, N. E. Clapp, and C. S. Daw, *Nonlinear Analysis of Machining Data*, ORNL/TM-13157, Oak Ridge National Laboratory, Oak Ridge, TN. (January 1996).

2. B. S. Berger, M. Rokni, and I. Minis, "The Nonlinear Dynamics of Metal Cutting," *Int. J. Engng. Sci.* **30,** 1433–1440 (1992).

3. S. T. S. Bukkapatnam, A. Lakhtakia, and S. R. T. Kumara, "Analysis of Sensor Signals Shows Turning on a Lathe Exhibits Low-Dimensional Chaos," *Phys. Rev. E* **52**, 2375–2387 (1995).

4. S. T. Chiriacescu, "Stability in the Dynamics of Metal Cutting," *Studies in Applied Mechanics* **22** Elsevier, New York (1990).

5. G. Giacomelli and A. Politi, "Relationship Between Delayed and Spatially Extended Dynamical Systems," *Phys. Rev. Lett.* **76** 2686–2689 (1996).

6. I. Grabec, "Chaos Generated by the Cutting Process," *Phys. Lett. A* **117,** 384–386 (1986).

7. I. Grabec, "Chaotic Vibrations and Acoustic Emission Caused by the Cutting Process," *Proc 8th Int. Acoustic Emissions Symp.*, Tokyo, Japan,1986, pp. 87–93.

8. I. Grabec, "Chaotic Dynamics of the Cutting Process," *Int. J. Mach. Tools Manufact.* **28,** 19–32 (1988).

9. C. Hualing and D. Depei, "A New Theoretical Model of Nonlinear Chatter in Cutting Process," *Proc. 11th Int'l Conf. Production Res. (ICPR)* 1991, pp. 932–936.

10. K. Jemielniak and A. Widota, "The Development of Frequency and Amplitude of Chatter Vibration," *Int. J. Mach. Tools Manufact.* **29**, 249–256 (1989).

11. R. I. King, "Historical Background," Chapter 1 in *Handbook of High-Speed Machining Technology*, R. I. King, ed., Chapman and Hall Publ., New York, 1985.

12. F. Koenigsberger and J. Tlusty, *Machine Tool Structures—Volume 1*, Pergamon Press, New York, 1970.

13. J. S. Lin and C. I. Weng, "A Nonlinear Dynamic Model of Cutting," *Int. J. Mach. Tools Manufact.* **30**, 53–64 (1990).

14. J. S. Lin and C. I. Weng, "Nonlinear Dynamics of the Cutting Process," *Int. J. Mech. Sci.* **8** 645–657 (1991).

15. F. C. Moon, "Chaotic Dynamics and Fractals in Material Removal Processes," Chapter 2 of *Nonlinearity and Chaos in Engineering Dynamics*, J. M. T. Thompson and S. R. Bishop (eds), John Wiley and Sons, Ltd (1994).

16. L. Qu, A. Xie, and X. Li, “Study and Performance Evaluation of Some Nonlinear Diagnostic Methods for Large Rotating Machines,” *Mech. Mach. Theory* **28**, 699–713 (1993).

17. G. Stépán, *Retarded Dynamical Systems: Stability and Characteristic Functions*, Pitman Res. Notes in Mathematics (Vol. 210) John Wiley and Sons (New York) 1989.

18. J. Tlusty, “Machine Dynamics,” Chapter 3 of *Handbook of High-Speed Machining Technology*, R.I. King (ed.), Chapman and Hall Publ., New York, 1985.

19. J. Tlusty and F. Ismail, “Basic Nonlinearity in Machining Chatter,” *Annals CIRP* **30** 299–304 (1981).

20. J. Tlusty and M. Poláček, “Experience with Analyzing Stability of Machine Tool Against Chatter,” *Proc. 9th MTDR Conf.*, Pergamon Press, 1968, pp. 521–570.

21. S. A. Tobias, *Machine-Tool Vibration*, John Wiley and Sons, New York, 1965.

22. Y. Ueda, H. Ohta, and H. B. Stewart, “Bifurcations in a System Described by a Nonlinear Differential Equation with Delay,” *Chaos* **4** 75–83 (1994).

23. D. B. Welbourn and J. D. Smith, “Dynamics of the Cutting Process,” Chapter 4 of *Machine-Tool Dynamics—An Introduction*, Cambridge University Press (1970).

24. D. B. Welbourn and J. D. Smith, “Chatter,” Chapter 5 of *Machine-Tool Dynamics—An Introduction*, Cambridge University Press (1970.

25. D. W. Wu and C. R. Liu, “An Analytical Model of Cutting Dynamics. Part 1: Model Building,” *J. Engng. for Industry* **107,** 107–111 (1985).

26. D. W. Wu and C. R. Liu, “An Analytical Model of Cutting Dynamics. Part 2: Verification,” *J. Engng. for Industry* **107**, 112–118 (1985).

27. S. Smith and J. Tlusty, “Stabilizing Chatter by Automatic Spindle Speed Regulation,” *Annals CIRP* **41** 433–436 (1992).

28. R. Teltz and M. A. Elbestawi, “Hierarchical, Knowledge-Based Control in Turning,” *Trans. ASME* **115** 122–132 (1993).

29. S. J. Schiff, K. Jerger, D. H. Duong, T. Chang, M. L. Spano, and W. L. Ditto, “Controlling Chaos in the Brain,” *Nature* **370**, 615–620 (1994).

30. V. In, S. E. Mahan, W. L. Ditto, and M. L. Spano, “Experimental Maintenance of Chaos,” *Phys. Rev. Lett.* **74**, 4420–4423 (1995).

31.Y.-C. Lai and C. Grebogi, “Converting Transient Chaos into Sustained Chaos by Feedback Control,” *Phys. Rev. E* **49**, 1094–1098 (1994).

32. Y. Nagai and Y.-C. Lai, “Selection of a Desirable Chaotic Phase Using Small Feedback Control,” *Phys. Rev. E* **51**, 3842–3848 (1995).

33. W. Yang, M. Ding, A. J. Mandell, and E. Ott, “Preserving Chaos: Control Strategies to Preserve Complex Dynamics with Potential Relevance to Biological Disorders,” *Phys. Rev. E* **51**, 102–110 (1995).

34. E. A. Jackson, *Perspectives of Nonlinear Dynamics*, Cambridge Univ. Press, Cambridge, 1991.

35. G. Chen and X. Dong, “From Chaos to Order—Perspectives and Methodologies in Controlling Chaotic Nonlinear Dynamical Systems,” *Int. J. Bifurc. and Chaos* **3**, 1363–1409 (1993).

36. T. Shinbrot, “Progress in the Control of Chaos,” *Adv. in Phys.* **44**, 73–111 (1995).

37. C. S. Daw, M. B. Kennel, C. E. A. Finney, and F. T. Connolly, “Observing and Modeling Nonlinear Dynamics in an International Combustion Engine,” *Phys. Rev. E*, **57**, 2811–2819 (1998).

38. R. W. Hamming, *Numerical Methods for Scientists and Engineers*, McGraw-Hill Book Company Publ., New York, 1962.

39. L. M. Hively, N. E. Clapp, C. S. Daw, W. F. Lawkins, and M. L. Eisenstadt, *Nonlinear Analysis of EEG for Epileptic Seizures*, ORNL/TM-12961, Oak Ridge National Laboratory, Oak Ridge, TN. (1995).

40. J. Alvarez-Ramirez, R. Garrido, and R. Femat, “Control of Systems with Friction,” *Phys. Rev. E* **51**, 6235–6238 (1995).

41. M. E. Bleich and J. E. S. Socolar, “Stability of Periodic Orbits Controlled by Time-Delay Feedback,” *Phys. Lett. A* **210**, 87 (1996).

42. A. Babloyantz, C. Lourenço, and J. A. Sepulchre, “Control of Chaos in Delay Differential Equations, in a Network of Oscillators and in Model Cortex,” *Physica D* **86**, 274–283 (1995).

43. K. Pyragas and Tamaševičius, “Experimental Control of Chaos by Delayed Self-Controlling Feedback,” *Phys. Lett. A* **180**, 99–102 (1993).

44. S. V. Drakunov and V. I. Utkin, “Sliding Mode Control in Dynamic Systems,” *Int. J. Control* **55**, 1029–1037 (1992).

45. S. V. Baida, “Unit Sliding Mode Control in Continuous and Discrete Time Systems,” *Int. J. Control* **57**, 1125–1132 (1993).

46. T. Kapitaniak, *Chaos in Systems with Noise*, Second Edition, World Scientific, Singapore (1990).

47. M. C. Mackey, A. Longtin, and A. Lasota, “Noise-Induced Global Asymptotic Stability,” *J. Stat. Phys.* **60**, 735–751 (1990).

48. T. Shinbrot, E. Ott, C. Grebogi, and J. A. Yorke, “Using Chaos to Direct Trajectories to Targets,” *Phys. Rev. Lett.* **65**, 3215–3218 (1990).

49. Y.-C. Lai, M. Ding, and C. Grebogi, “Controlling Hamiltonian Chaos,” *Phys. Rev. E* **47**, 86–92 (1993).

50. M. Ding, E. Ott, and C. Grebogi, “Controlling Chaos in a Temporally Irregular Environment,” *Physica D* **74**, 386–394 (1994).

51. G. Malescio, “Effects of Noise on Chaotic One-Dimensional Maps,” *Phys. Lett. A* **218**, 25–29 (1996).

52. G. Malescio, “Noise and Synchronization in Chaotic Systems,” *Phys. Rev. E* **53**, 6551–6554 (1996).

53. L. Arnold, “Stabilization by Noise Revisited,” *Z. Angew. Math.* **70**, 235–246 (1990).

54. L. Arnold and P. Boxler, “Additive Noise Turns A Hyperbolic Fixed Point into a Stationary Solution,” preprint (1996).

55. J. P. Crutchfield, J. D. Farmer, and B. A. Huberman, “Fluctuations and Single Chaotic Systems,” *Phys. Rep.* **92**, 45–82 (1982).

56. G. Boffetta, G. Paladin, and A. Vulpiani, “Strong Chaos Without Butterfly Effect in Dynamical Systems with Feedback,” *J. Phys. A* **29**, 2291–2298 (1996).

57. J. R. Pratt and A. H. Nayfeh, “Boring Bar Chatter Control Using Two Axes Active Vibration Absorber Scheme,” *Noise-Con 97*, pp. 313–324, (Pennsylvania State Univ.) 15–17 June 1997.

58. J. Pratt and A. H. Nayfeh, “Active Vibration Control for Chatter Suppression,” *AIAA-97-1210*, pp. 623–633 (Amer. Inst. Aeronautics & Astronautics) 1997.

59. D. Browning, “Pro-Active Chatter Reduction,” *Modern Machine Shop*, 86–92 (June 1998).

60. L. M. Hively, “Data-Driven Nonlinear Technique for Condition Monitoring,” *Proc. Maintenance and Reliability Conf.*, Vol. 1, pp. 16.01ff (Univ. of Tennessee).

61. L. M. Hively and E. S. Ng, “Integrated method for chaotic time series analysis,” U.S. Patent pending (1998).

62. L. M. Hively and P. C. Gailey, submitted for publication (1998).

DISTRIBUTION

1. M. A. Akerman
2. J. Barhen
3. W. E. Barkman
4–6. N. E. Clapp
7–8. C. S. Daw
9. E. C. Fox
10–13. L. M. Hively
14. R. F. Holdaway
15. G. T. Mays
16. L. E. Parker
17–18. V. A. Protopopescu
19. D. B. Reister
20. S. C. Robinson
21. R. M. Schilling, Jr.
22. J. F. Thomas
23. D. E. Welch
24. T. Zacharia
25. Central Research Library
26–27. ORNL Laboratory Records (OSTI)
28. Laboratory Records—RC